

# Microrobot Vascular Parkour: Analytic Geometry–based Path Planning with Real-time Dynamic Obstacle Avoidance

Yanda Yang<sup>1</sup>, Max Sokolich<sup>1</sup>, Fatma Ceren Kirmizitas<sup>1,2</sup>, Sambaeta Das<sup>1\*</sup>,  
Andreas A. Malikopoulos<sup>3</sup>

<sup>1</sup>Department of Mechanical Engineering, University of Delaware, Newark 19716, USA.

<sup>2</sup>Department of Animal and Food Sciences, University of Delaware, Newark 19716, USA.

<sup>3</sup>School of Civil and Environmental Engineering, Cornell University, Ithaca, NY 14853, USA.

\*Corresponding author. Email: samdas@udel.edu

**Autonomous microrobots in blood vessels could enable minimally invasive therapies, but navigation is challenged by dense, moving obstacles. We propose a real-time path planning framework that couples an analytic geometry global planner (AGP) with two reactive local escape controllers, one based on rules and one based on reinforcement learning, to handle sudden moving obstacles. Using real-time imaging, the system estimates the positions of the microrobot, obstacles, and targets and computes collision-free motions. In simulation, AGP yields shorter paths and faster planning than weighted A\* (WA\*), particle swarm optimization (PSO), and rapidly exploring random trees (RRT), while maintaining feasibility and determinism. We extend AGP from 2D to 3D without loss of speed. In both simulations and experiments, the combined global planner and local controllers reliably avoid moving obstacles and reach targets. The average planning time is 40 ms per frame, compatible with 25 fps image acquisition and real-time**

**closed-loop control. These results advance autonomous microrobot navigation and targeted drug delivery in vascular environments.**

## INTRODUCTION

Microscale robotics is emerging as a platform for precise, minimally invasive therapies, especially targeted drug delivery (1, 2). Conventional delivery routes (oral or intravenous) often lack spatial specificity, leading to off-target effects and reduced efficacy (3). Recent magnetic and bio-inspired microrobots can carry therapeutic payloads directly to sites of disease (e.g., tumors, inflamed tissue, occlusions) (4–6). Their small size enables navigation in confined spaces with noninvasive actuation and precise targeting, simplifying otherwise complex procedures (7, 8) and opening avenues in regenerative medicine (9).

Because micrometer agents cannot house actuators, sensors, or processors onboard, they are propelled and steered by external fields. A broad set of actuation modalities has been explored: magnetic and electric fields, chemical reactions, acoustics, and light-responsive materials (10–15). Chemical actuation can raise biocompatibility concerns, and optical methods are limited by penetration depth in tissue. Magnetic actuation avoids these constraints and has therefore become a leading choice for biomedical microrobotics (16–20).

Effective use of magnetic microrobots depends on reliable path planning and obstacle avoidance in blood vessels (21–26). Existing planners span optimization (e.g., particle swarm optimization, PSO) (27, 28), graph search (e.g.,  $A^*$ ) (29, 30), and sampling (e.g., rapidly exploring random trees, RRT) (31–34). Each has drawbacks for time-critical navigation: PSO can converge slowly and inconsistently due to multi-particle exploration;  $A^*$  can incur heavy search costs in large or high-dimensional grids; and RRT is stochastic, with variable quality and no optimality guarantee.

A central challenge is real-time planning in the presence of dynamic obstacles (35, 36). In blood vessels, microrobots frequently encounter moving red blood cells, protein aggregates, and other debris, demanding rapid, reactive decisions. Some dynamic obstacle avoidance methods have been developed in recent years, such as radar-based methods (37, 38), artificial potential fields (22), Dynamic Window Approach (DWA) (39), fuzzy logic (40), and learning-based policies (41, 42). But there are still some unresolved issues. Extensions of traditional path planning methods often fail

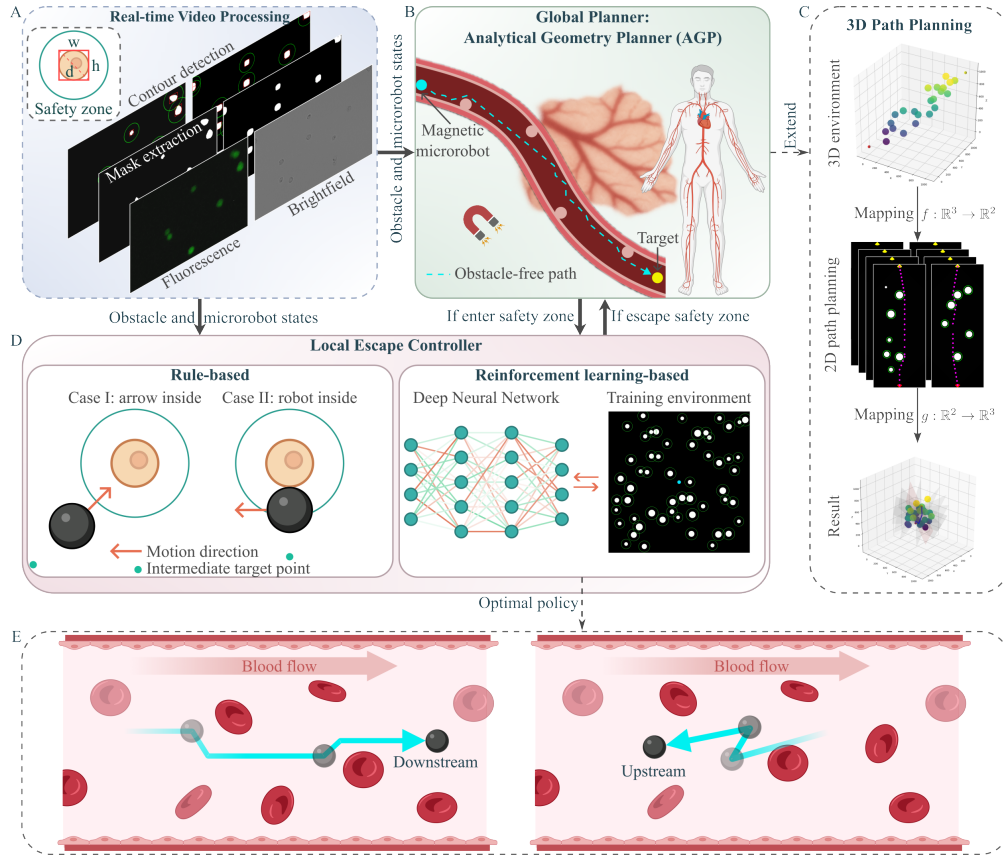


**Figure 1: Framework for microrobot navigation and dynamic obstacle avoidance in blood vessels.** (A) Real-time video processing and extracting microrobot and obstacle states, including safety zones. (B) Analytic geometry planner (AGP) computes a collision-free path to the target. When the microrobot enters a safety zone, control switches to the local escape module. (C) Extension to three dimensions: mapping from the three-dimensional environment to the two-dimensional imaging plane for planning and lifting the planned path back to three dimensions. (D) Local escape controllers: a rule-based controller and a reinforcement learning-based controller. When the microrobot escapes a safety zone, AGP replans the global path. (E) The microrobot moves downstream and upstream in a blood vessel while avoiding moving red blood cells.

to meet real-time computational requirements due to inherent algorithmic complexity. Currently, most prior work typically targets low-speed swarms, and real-time planning for high-speed rolling microrobots remains underexplored. Moreover, most prior work evaluates their methods in simulated or single-scenario environments with a simple dynamic obstacles setting, which limits insight into how these methods perform in realistic, complex, dynamic settings and prevents evaluation of their generalization across diverse conditions.

To address these issues, we introduce a real-time framework for autonomous microrobot navigation (Figure 1). A deterministic analytic geometry-based global planner (AGP) produces a collision-free path without search or sampling. Two complementary local escape controllers, one rule-based and one reinforcement learning-based, handle sudden, short-range interactions with moving obstacles. The system processes a live microscope video stream into frames, generates masks from them, and identifies contours to extract details such as obstacle dimensions, safe zones, and location coordinates. Given the microrobot's current position and a predefined target point, the AGP calculates the near-optimal collision-free path based on the latest frame information. When a dynamic obstacle appears and the microrobot enters the safety zone of the obstacle, the local escape controller activates and takes over. Once the microrobot successfully escapes the safe zone, the AGP replans the global path. This iterative process continues until the target is reached. The contributions of our work are as follows:

1. A real-time navigation framework that couples a deterministic global planner (AGP) with two reactive local controllers (rule-based and reinforcement learning-based). We validate the system in simulation and vascular-like microfluidic environments with realistic dynamic obstacles.
2. A fast, deterministic global planner: AGP yields feasible paths and outperforms WA\*, PSO, and RRT in path length and planning time. With the local controllers, the average planning time is 40 ms per frame, satisfying closed-loop real-time operation.
3. A 3D extension of AGP that preserves computational speed, enabling real-time planning in complex spatial geometries.
4. A reinforcement learning controller dedicated to short-range dynamic avoidance. Restricting

learning to this local task improves sample efficiency and robustness, while the modular design keeps global plans interpretable and easily re-plannable.

5. A deterministic intermediate waypoint controller based on relative microrobot and obstacle geometry. It requires no training, is human-readable and verifiable, and provides predictable responses in scenarios where learned policies might generalize poorly.

We first evaluate the framework across diverse dynamic simulations, including vascular phantoms, to assess versatility and robustness. We then integrate it with a magnetic control system and demonstrate collision-free navigation in microfluidic chips containing dynamic obstacles (silica particles and human red blood cells), validating reliable operation under realistic conditions.

## RESULTS

### Environmental Information

The cell–microrobot environment can be known by fluorescence or bright-field imaging. From each frame of the real-time video stream, image processing extracts the positions and sizes of all objects in the environment.

For every frame, we convert the image from BGR to HSV and to grayscale for contour detection, as shown in Figure S4. Let the image be a matrix  $\mathbf{I} \in \mathbb{R}^{H \times W}$  with height  $H$  and width  $W$ . Pixels are treated as Cartesian coordinates  $(x, y)$  with  $x \in \{0, 1, \dots, W - 1\}$  and  $y \in \{0, 1, \dots, H - 1\}$ . Thresholding produces a binary mask from which obstacle contours are found. For each contour, we compute an axis-aligned bounding box and its center  $\mathbf{c}_i = (x_{c,i}, y_{c,i})^\top$ . Let  $\mathcal{I} = \{1, 2, \dots, N\}$  index the  $N$  detected obstacles, and stack the centers as

$$C = \begin{bmatrix} \mathbf{c}_1^\top \\ \mathbf{c}_2^\top \\ \vdots \\ \mathbf{c}_N^\top \end{bmatrix} \in \mathbb{R}^{N \times 2}.$$

For planning, we inflate obstacles by the microrobot radius and treat the microrobot as a point, which facilitates subsequent calculations and simplifies the problem. Cell shapes are not perfectly

circular, so we approximate each cell diameter by the diagonal of its bounding box. The safety zone radius for obstacle  $i \in \mathcal{I}$  is

$$d_i = \sqrt{w_i^2 + h_i^2}, \quad (1)$$

$$r_i = \frac{1}{2}d_i + R, \quad (2)$$

where  $w_i$  and  $h_i$  are the box width and height,  $R$  is the microrobot radius, and the box is centered at  $\mathbf{c}_i$ . Collect the radii as  $\mathbf{r} = [r_1, r_2, \dots, r_N]^\top \in \mathbb{R}^N$ .

## Analytic Geometry-based Planner (AGP)

We seek the shortest feasible path from the start point  $\mathcal{S} = (x_s, y_s)$  (red) to the end point  $\mathcal{E} = (x_e, y_e)$  (yellow) that avoids the safety zones (green) around detected obstacles (white), as illustrated in Figure 2(A)I. Let  $\mathcal{K} = \{1, \dots, K\}$  index  $K$  primary nodes and  $\mathcal{J} = \{1, \dots, J\}$  index  $J$  intermediate waypoints with  $J \gg K$ . Stack node coordinates as

$$V = [v_1, \dots, v_K]^\top \in \mathbb{R}^{K \times 2}, \quad v_k = (x_{v,k}, y_{v,k})^\top,$$

and waypoint coordinates as

$$W = [w_1, \dots, w_J]^\top \in \mathbb{R}^{J \times 2}, \quad w_j = (x_{w,j}, y_{w,j})^\top.$$

The endpoints  $\mathcal{S}$  and  $\mathcal{E}$  are included as the first and last entries of both  $V$  and  $W$ . AGP is initialized by the straight line ideal path  $\mathcal{S} \rightarrow \mathcal{E}$  (orange dotted line).

**Obstacle pruning.** Define  $\mathbf{s} = (x_s, y_s)^\top$ ,  $\mathbf{e} = (x_e, y_e)^\top$ , and  $\mathbf{d} = \mathbf{e} - \mathbf{s}$ . The ideal path is the parametric line  $\mathbf{s} + \tau \mathbf{d}$ ,  $\tau \in \mathbb{R}$ . Let  $\mathcal{I} = \{1, \dots, N\}$  index all detected obstacles, each with center  $\mathbf{c}_i = (x_{c,i}, y_{c,i})^\top$  and safety zone radius  $r_i$ .

First, project  $\mathbf{c}_i$  onto the ideal path,

$$t_i = \frac{(\mathbf{c}_i - \mathbf{s}) \cdot \mathbf{d}}{\|\mathbf{d}\|^2}, \quad (3)$$

and retain only obstacles with  $0 \leq t_i \leq 1$  so that the orthogonal foot  $\mathbf{g}_i = \mathbf{s} + t_i \mathbf{d}$  lies between  $\mathcal{S}$  and  $\mathcal{E}$ . Geometrically, this retains only the obstacles located in the light orange shaded area, as shown in Figure 2(A)II. Second, discard any obstacle whose center-to-foot distance exceeds a scaled radius:

$$\|\mathbf{c}_i - \mathbf{g}_i\| > \alpha r_i \quad \Rightarrow \quad \text{discard}, \quad \alpha > 0. \quad (4)$$

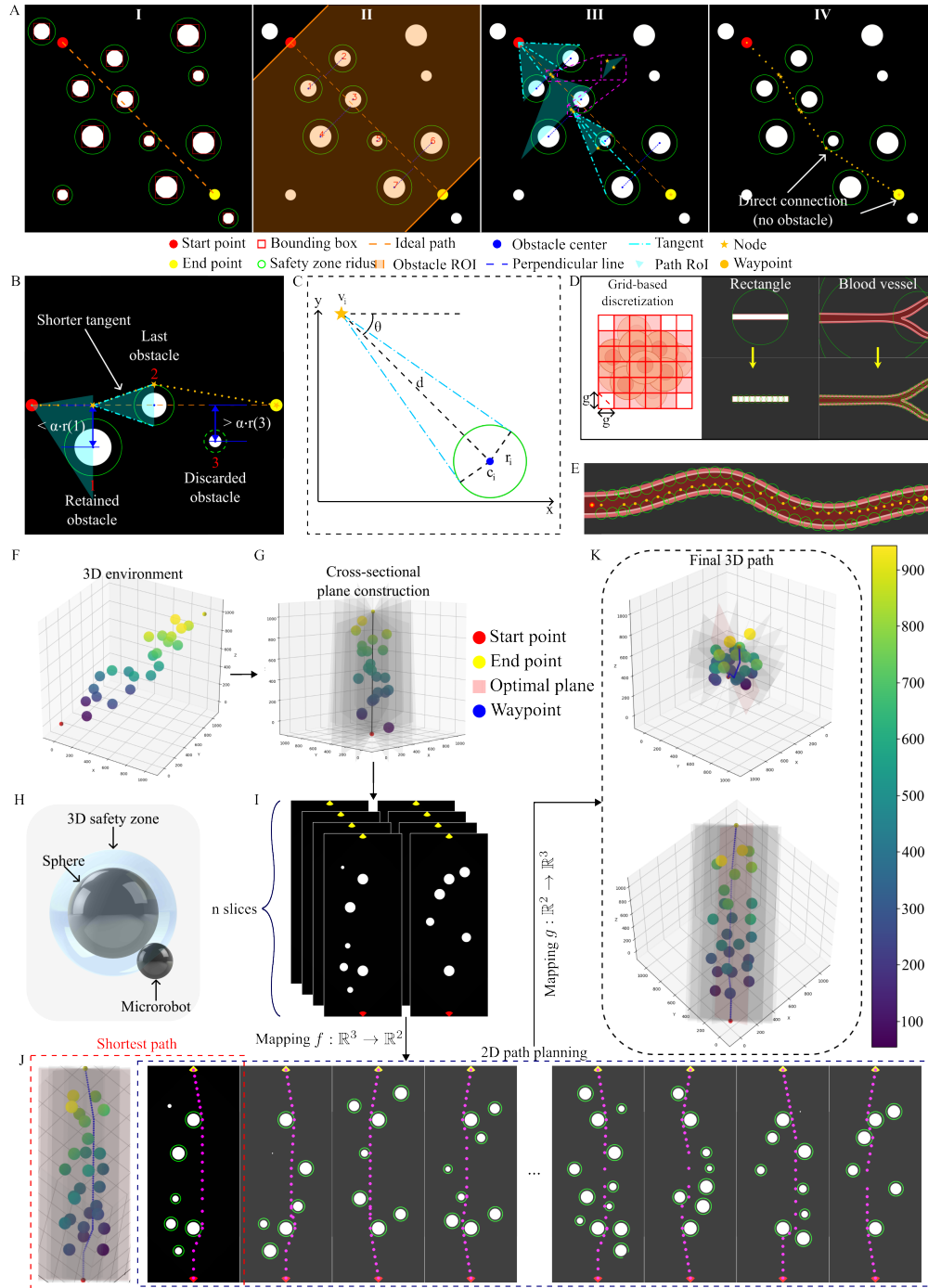


**Figure 2: Analytic geometry-based Planner (AGP).** (A) The graphical process of AGP to derive a collision-free path. (B) Obstacle selection for  $\alpha = 3$  (retained vs. discarded). (C) Construction of tangents from node  $v_i$  to obstacle  $i$ 's safety circle. (D) Grid-based discretization of a noncircular obstacle bounding box and resulting safety zones. (E) Solution in a vascular phantom with boundary obstacles (vessel walls). (F-K) 3D extension of AGP

Equivalently, AGP keeps obstacles whose safety zones intersect the strip of half-width  $\alpha r_i$  around the ideal path. This rule tends to keep large obstacles even when slightly off path, and to keep small obstacles only when close to the path. As shown in Figure 2(B), obstacle 1 is retained and obstacle 3 is discarded. Let  $\mathcal{I}' \subseteq \mathcal{I}$  be the retained indices with  $M = |\mathcal{I}'|$ . Collect the foot points as

$$G = [\mathbf{g}_i]_{i \in \mathcal{I}'}^\top \in \mathbb{R}^{M \times 2}.$$

The surviving obstacles are marked by blue dots at  $\mathbf{c}_i$  and green circles of radius  $r_i$ .

**Ordering and perpendicular families.** Sort the rows of  $C$  (obstacle centers),  $G$  (foot points),  $\mathbf{r}$  (radii), and  $\mathbf{e}_p$  (defined below) by increasing  $x$ -coordinate of the foot points,  $x_{g,i}$ . Let the slope of the ideal path be  $k_o = (y_e - y_s)/(x_e - x_s)$  when  $x_e \neq x_s$ . The family of lines through each  $\mathbf{c}_i$  that are perpendicular to the ideal path has slope  $k_p = -1/k_o$  and intercept

$$e_{p,i} = y_{c,i} - k_p x_{c,i}. \quad (5)$$

Thus each primary node  $v_i = (x_{v,i}, y_{v,i})^\top$  is constrained to

$$y_{v,i} = k_p x_{v,i} + e_{p,i}. \quad (6)$$

For the vertical ideal-path case ( $x_e = x_s$ ), replace the slope form by the vector constraint  $(v_i - \mathbf{c}_i) \cdot \mathbf{d} = 0$ .

**Node advancement via tangents.** Collision avoidance with obstacle  $i$  is enforced by

$$r_i^2 \leq \|v_j - \mathbf{c}_i\|^2 \quad \text{for all relevant } i, \quad (7)$$

namely, each node must lie outside every safety zone. For each current node  $v_i$ , compute the tangents from  $v_i$  to the two nearest safety circles, as shown in Figure 2(C)). Let

$$\theta_i = \text{atan2}(y_{c,i} - y_{v,i}, x_{c,i} - x_{v,i}), \quad d_i = \|\mathbf{c}_i - v_i\|,$$

with the feasibility condition  $d_i > r_i$ . The two tangent directions relative to  $\theta_i$  have slopes

$$m_{1,2} = \tan\left(\theta_i \pm \arcsin\frac{r_i}{d_i}\right). \quad (8)$$

Together with the line through the next foot point  $\mathbf{g}_{i+1}$  that is parallel to the perpendicular family (slope  $k_p$ ), these tangents form a triangle of interest (light blue in Figure 2(A)III). To place the next node  $v_{i+1}$ , drop a perpendicular from  $v_i$  to the side of that triangle. If the foot point lies outside all safety zones, accept it as  $v_{i+1}$ ; otherwise, take the intersection of the shortest valid tangent with that side as  $v_{i+1}$ . Remove the obstacle closest to  $v_i$  from the active set and repeat with the two obstacles nearest  $v_{i+1}$ . If only one obstacle remains (for example, obstacle 2 in Figure 2(B)), choose the shorter tangent. If the straight segment  $v_i \rightarrow \mathcal{E}$  has at most one intersection with the safety circle, set  $v_{i+1} = \mathcal{E}$  (Figure 2(A)IV).

After all nodes are selected, store them in  $V = [v_1, \dots, v_K]^\top \in \mathbb{R}^{K \times 2}$ . Insert additional waypoints along each segment in proportion to segment length and collect them in  $W = [w_1, \dots, w_J]^\top \in \mathbb{R}^{J \times 2}$ . Figure S5(A) shows more solution paths from AGP.

**Noncircular obstacles and boundaries.** To handle elongated shapes and vessel walls, compute each obstacle’s bounding box and discretize it into square cells of side length  $g$  (Figure 2(D)). Retain cells that contain contour pixels, group connected cells into sub-contours, and assign each a safety zone

$$d_{\text{cell}} = \sqrt{2} g, \quad r_{\text{cell}} = \frac{1}{2} d_{\text{cell}} + R, \quad (9)$$

where  $R$  is the microrobot radius. Replacing one large safety zone with multiple smaller ones increases free space in boundary-defined scenes. Figure 2(D) shows the finer safety zones after discretization, and Figure 2(E) shows a resulting path in a curved vascular phantom. More results can be found in Figure S5(D) and (E).

**Summary.** By pruning obstacles with projection and distance tests, then advancing nodes using tangents and perpendiculars, AGP constructs a collision-free path from  $\mathcal{S}$  to  $\mathcal{E}$  with primary nodes and dense waypoints suitable for closed-loop execution. The modification of the AGP solution path can be found in Supplementary Text. Algorithm 3 describes the analytic geometry-based path planning method.

## Performance Evaluation of Global Planner

We compare our analytic geometry planner (AGP) with particle swarm optimization (PSO), rapidly exploring random trees (RRT), and weighted A\* (WA\*) in static simulated environments. All other algorithms were implemented (see Supplementary Text) and use the same safety zone definition. Figure 3(A) shows example solution paths from the four algorithms in the same scenario. We evaluate two metrics (path length and computation time) across multiple environments.

To ensure a fair comparison, we generated six  $2000 \times 2000$  px arenas with 10, 20, 30, 40, 50, and 60 circular obstacles (radius 50 px) to mimic a crowded cellular scene (Figure 3(B)). Each obstacle has the same safety zone radius of 75 px. The start (red) is fixed at the upper-left corner and the end (yellow) at the lower-right corner. Each method is run 10 times per environment; we record computation time and the resulting path length on every run.

For AGP, obstacles  $i$  whose centers  $\mathbf{c}_i$  lie farther than  $\alpha r_i$  from the ideal path are pruned; we use  $\alpha = 6$  in all scenarios. For PSO, the path is parameterized by 50 waypoints with a damping factor  $w = 0.9$ . In the 10–30 obstacle cases, we use population size  $P = 100$  and generations  $K = 50$ ; for 40–60 obstacles, we increase to  $P = 200$  with  $K = 50$  to maintain feasibility. For RRT, a step size of  $\Delta s = 50$  px with a goal tolerance of  $\delta_{\text{tol}} = 50$  px is used to guide tree expansion and determine the proximity of the goal. For WA\*, the weighting parameter  $w$  is set to 1.5 to balance the heuristic and cost function, improving the search efficiency.

Figure 3(C) summarizes path lengths. RRT consistently yields the longest paths with high variance; even its best runs are longer than those from the other methods. PSO occasionally finds the shortest path but is unstable, frequently returning much longer alternatives, which raises its average length above AGP and WA\*. AGP and WA\* produce deterministic solutions without run-to-run variation across all six scenarios. The only exception in our tests is scenario 4, where AGP (2872.26 px) is slightly longer than WA\* (2862.67 px); in all other cases, AGP is shorter.

Regarding the computation time, as shown in Figure 3(D), AGP is consistently fast, remaining below 0.2 s in all scenarios. PSO shows strong dependence on obstacle count, rising from about 1.4 s to roughly 21 s at 60 obstacles. RRT averages around 0.5 s with modest variability. WA\* is near 0.2 s for 10 and 20 obstacles, and then trends to approximately 0.3 s, 0.7 s, and 0.3 s for 30, 40, and 50 obstacles, respectively; at 60 obstacles its time increases to about 5.2 s but remains stable

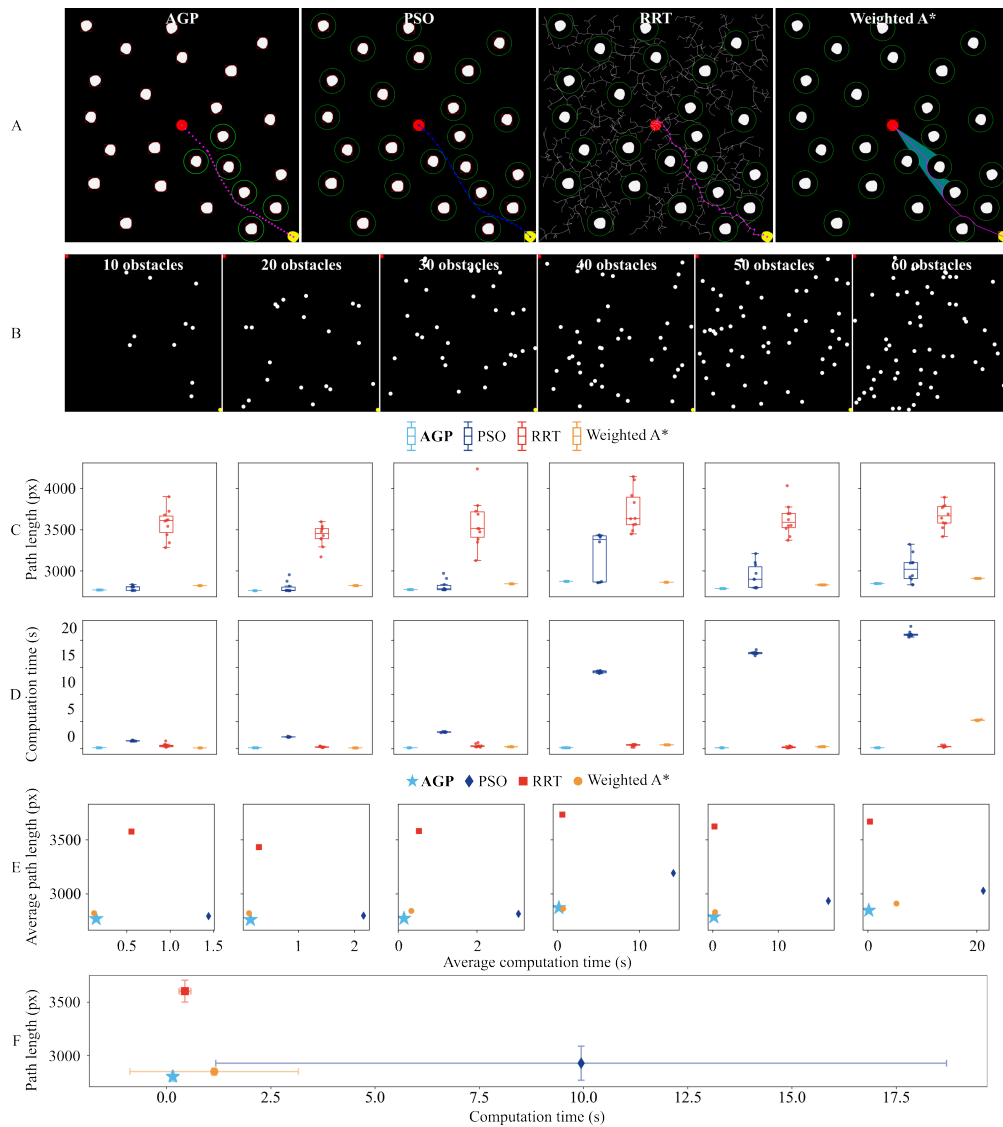


**Figure 3: Performance evaluation of global planners.** (A) Example solution paths from AGP, PSO, RRT, and WA\* in the same static environment (start: red, end: yellow). (B) Six test arenas ( $2000 \times 2000$  px) with 10–60 circular obstacles. (C) Path length over 10 runs per method and environment (dots show individual runs). (D) Computation time for the same runs. (E) Trade-off view: mean path length versus mean computation time for each method in each environment (closer to the origin is better). (F) Aggregate comparison across all environments, highlighting AGP’s combination of short paths and low computation time.

across runs.

Figure 3(E) plots the mean path length and computation time over 10 runs per method and environment. Across all six scenarios, AGP lies closest to the origin, indicating the best joint trade-off. Figure 3(F) aggregates results across environments: AGP is both fast and insensitive to obstacle count, while also yielding the shortest paths in most cases. These findings support AGP as a stable and efficient global planner for this task.

### 3D Extension of AGP

We extend AGP to three dimensions by slicing the 3D space with a family of cross-sectional planes around the ideal path (Figure 2(F–G)). Let  $\mathcal{S} = (x_s, y_s, z_s)^\top$  and  $\mathcal{E} = (x_e, y_e, z_e)^\top$ , and define

$$\mathbf{d} = \mathcal{E} - \mathcal{S}, \quad \hat{\mathbf{d}} = \mathbf{d} / \|\mathbf{d}\|.$$

Choose any unit vector  $\mathbf{q}_0$  orthogonal to  $\hat{\mathbf{d}}$ . For  $i = 1, \dots, n$ , set  $\phi_i = 2\pi(i - 1)/n$  and rotate  $\mathbf{q}_0$  about  $\hat{\mathbf{d}}$  to obtain  $\mathbf{q}_i$ ; define the plane basis

$$\mathbf{e}_1 = \hat{\mathbf{d}}, \quad \mathbf{e}_2 = \mathbf{q}_i, \quad \mathbf{n}_i = \mathbf{e}_1 \times \mathbf{e}_2,$$

and the plane

$$\mathcal{P}_i = \{\mathcal{S} + u \mathbf{e}_1 + v \mathbf{e}_2 : u, v \in \mathbb{R}\}.$$

Each obstacle is modeled as a sphere with center  $\mathbf{C}$  and radius  $R_i$ ; the microrobot has radius  $R$ , so the 3D safety zone radius (Figure 2(H)) is

$$r_i^{3D} = R_i + R.$$

For plane  $\mathcal{P}_i$ , let

$$\delta_i = (\mathbf{C} - \mathcal{S}) \cdot \mathbf{n}_i, \quad d_i = |\delta_i|.$$

If  $d_i \leq r_i^{3D}$ , the intersection is a circle on  $\mathcal{P}_i$  with center

$$\mathbf{P} = \mathbf{C} - \delta_i \mathbf{n}_i$$

and radius

$$r_{\text{int}} = \sqrt{(r_i^{3D})^2 - d_i^2}.$$

Define the projection map and its inverse using the plane basis:

$$f : \mathbb{R}^3 \rightarrow \mathbb{R}^2, \quad f(\mathbf{P}) = \begin{pmatrix} u \\ v \end{pmatrix} = \begin{pmatrix} \mathbf{e}_1^\top (\mathbf{P} - \mathcal{S}) \\ \mathbf{e}_2^\top (\mathbf{P} - \mathcal{S}) \end{pmatrix}, \quad g : \mathbb{R}^2 \rightarrow \mathbb{R}^3, \quad g(u, v) = \mathcal{S} + u \mathbf{e}_1 + v \mathbf{e}_2.$$

We plan on each 2D slice with AGP (Figure 2(I)), producing waypoints  $\{w_{i,1}, \dots, w_{i,k_i}\} \subset \mathbb{R}^2$  and length

$$L_i = \sum_{j=1}^{k_i-1} \|w_{i,j+1} - w_{i,j}\|.$$

We select the optimal plane

$$i^* = \arg \min_{1 \leq i \leq n} L_i$$

and reconstruct the 3D path by lifting  $\{w_{i^*,j}\}$  via  $g$ , as in Figure 2(J–K). In the example shown, slicing, planning, and reconstruction complete in approximately 0.3 s, which indicates feasibility for real-time operation in dynamic 3D environments. Algorithm 4 describes the 3D extension of AGP.

## Rule-based Local Escape Controller

To handle dynamic obstacles, we use a rule-based local escape controller that is instantly deployable and highly interpretable. It requires no training or data collection, and each rule is easy to inspect and debug. Let

$$\mathbf{m} = (x_m, y_m)^\top, \quad \mathbf{a} = (x_a, y_a)^\top, \quad \mathbf{c}_i = (x_{c,i}, y_{c,i})^\top$$

denote the microrobot center, the tip of the motion direction arrow, and the center of obstacle  $i$ , respectively (Figure 4(A)). We consider two cases.

**Case I.** If the arrow tip  $\mathbf{a}$  enters the safety zone of obstacle  $i$ , reflect  $\mathbf{a}$  across the microrobot center to obtain a temporary intermediate target:

$$\mathbf{a}' = 2\mathbf{m} - \mathbf{a}.$$

**Case II.** If the microrobot center  $\mathbf{m}$  enters the safety zone of obstacle  $i$ , reflect the obstacle center across  $\mathbf{m}$  to obtain the temporary target:

$$\mathbf{c}'_i = 2\mathbf{m} - \mathbf{c}_i.$$

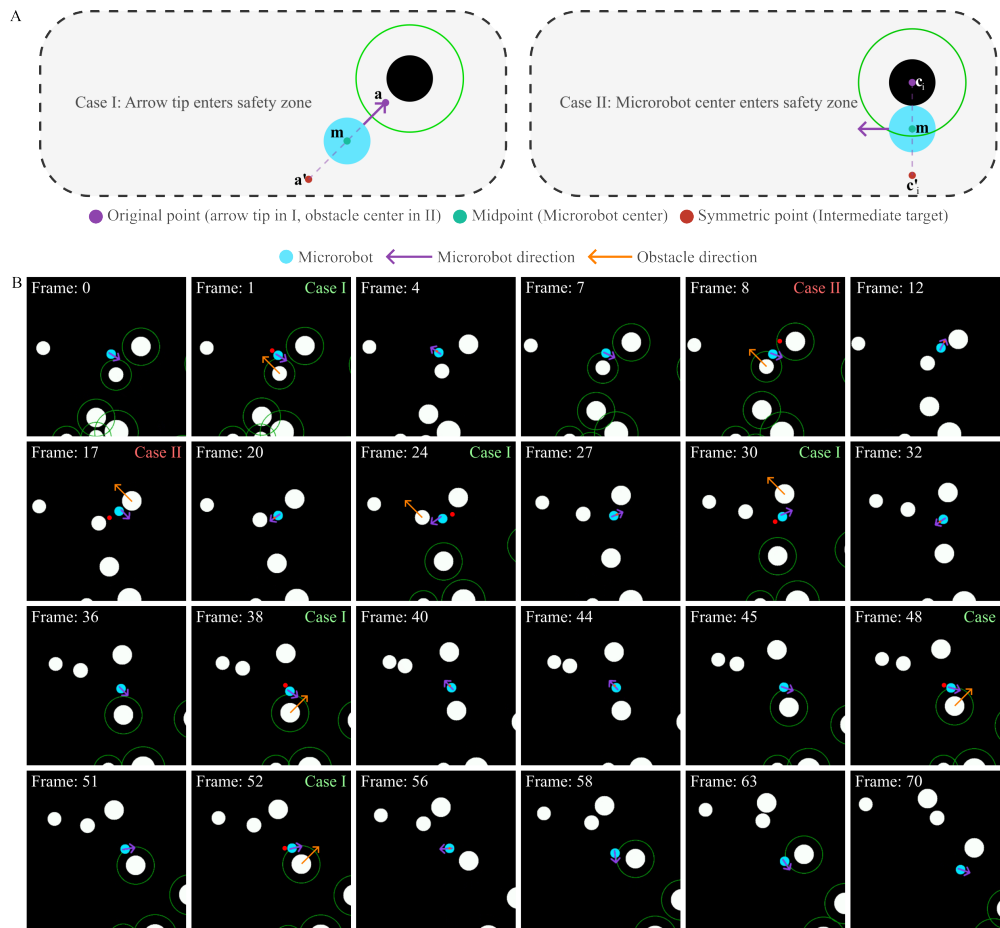


**Figure 4: Rule-based local escape controller.** (A) Two predefined cases for generating a temporary intermediate target. Case I: The arrow tip enters a safety zone, so its reflection across the microrobot center is used. Case II: The microrobot center enters a safety zone, so the reflection of the obstacle center is used. (B) Simulated sequence of dynamic obstacle avoidance using the rule-based controller. The purple arrow shows microrobot direction; the orange arrow shows obstacle direction; red dots are intermediate targets. Labels indicate which case is active.

In either case, the controller commands the microrobot to move toward the chosen symmetric point for  $\Delta$  frames, where  $\Delta \in \mathbb{N}$ , and then re-evaluates the two cases.

Figure 4(B) and Movie S4 show a simulated sequence. The purple arrow indicates the microrobot’s motion direction, and its length is

$$L_a = v_m + v_{c,\max},$$

where  $v_m$  is the microrobot speed,  $v_{c,i}$  is the speed of obstacle  $i$ , and  $v_{c,\max} = \max_i v_{c,i}$ . This one frame lookahead makes the arrow tip a forecast of the next microrobot position. The orange arrow indicates obstacle motion. When a red intermediate target appears, the upper-right label displays “Case I” or “Case II” to indicate which case is active. These targets update dynamically, so the microrobot moves toward the newest red point and then resumes heading to the final target. The controller avoids every moving obstacle in this scenario, which shows that the two simple predefined rules are sufficient for effective dynamic avoidance.

## Reinforcement Learning-based Local Escape Controller

Rule-based heuristics are instantly deployable and interpretable, but they can be suboptimal. Reinforcement learning can discover near-optimal local strategies from experience. We therefore train a controller that focuses exclusively on short-range avoidance. Because it attends only to the local neighborhood, the model does not observe the global goal, which reduces training complexity.

**Architecture and loop.** Figure 5(A) shows the DQN loop. A deep Q-network takes a 16-dimensional observation and passes it through two hidden layers (512 and 256 units) to produce nine action values; the policy is the greedy selection  $\pi(o) = \arg \max_a Q_\theta(o, a)$ . At each step, the agent observes the state, selects an action with  $\varepsilon$ -greedy exploration, and receives the next state and reward.

**Simulation environment.** The workspace is a  $W \times H$  rectangle with a microrobot of radius  $R$  and two obstacle sets:  $N_d$  dynamic and  $N_s$  static circles (Figure 5(A)). Each episode starts with the microrobot at the arena center. To emulate the role of the global AGP planner, the microrobot initially chooses one of eight compass directions ( $45^\circ$  increments) uniformly at random and moves

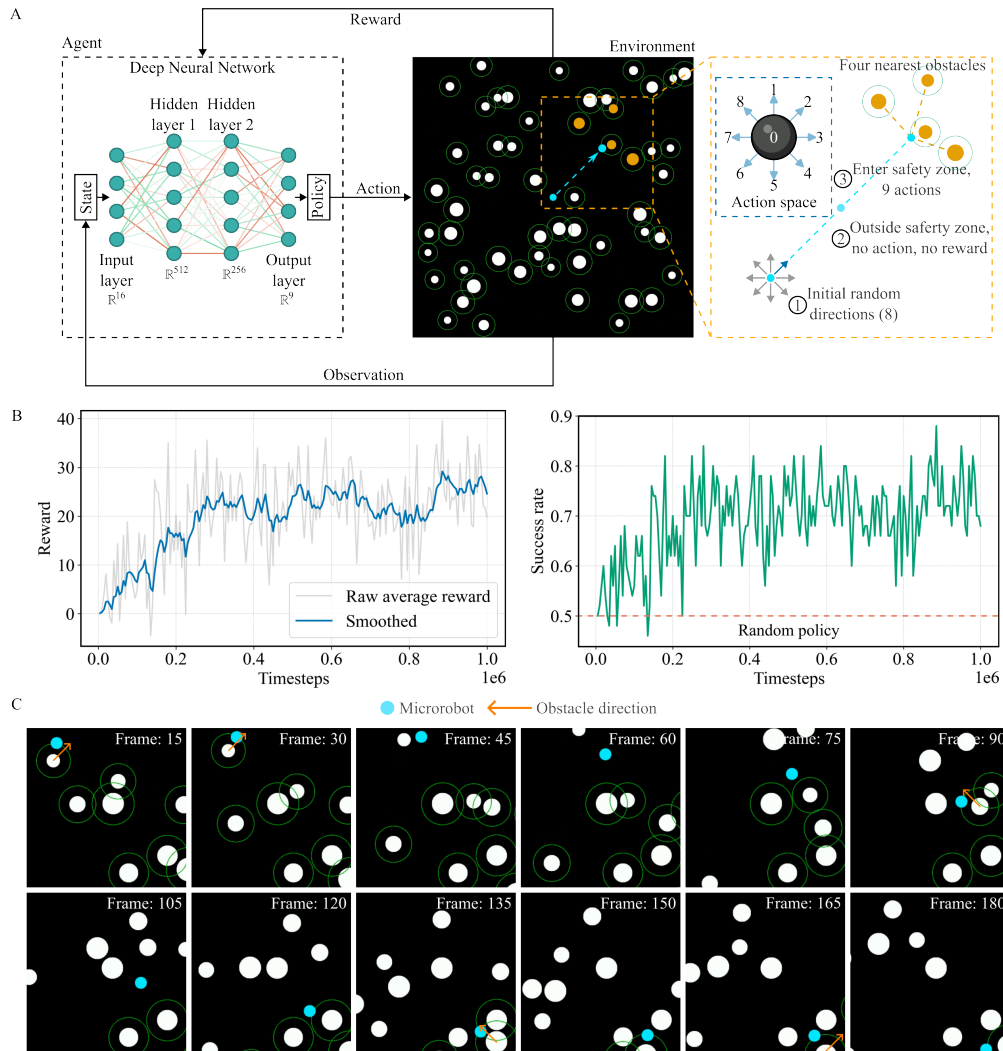


**Figure 5: Reinforcement learning–based local escape controller.** (A) DQN training loop and environment: a 16-dimensional observation (four nearest obstacles: relative position and velocity) feeds a two-layer Q-network (512 and 256 units) that outputs nine action values; actions are selected with an  $\varepsilon$ -greedy policy. The agent acts only inside safety zones; outside, no action and no reward are issued. (B) Training curves over one million environment steps: smoothed episode return (left) and success rate (right). The dashed line marks the random-policy baseline at 50%. (C) Simulated sequence of dynamic obstacle avoidance using the RL-based controller.

straight at speed  $v_m$ . During this “global” phase, while outside all safety zones, no RL actions or rewards are issued. When the microrobot first enters any safety zone, control switches to the learned policy. Movie S4 shows the training environment.

Each obstacle  $i$  has a physical radius  $r_i$  and a safety zone radius

$$r_i^{\text{sim}} = r_i + R + \delta, \quad \delta = v_m + v_{c,\max}, \quad v_{c,\max} = \max_i v_i, \quad (10)$$

which buffers for the one-step motion of the microrobot and the fastest obstacle. Dynamic obstacles move at constant speed  $v_i$  along one of eight directions and bounce elastically from walls and other obstacles; static obstacles have  $v_i = 0$ .

**Actions and observations.** At each control interval  $\Delta$ , the agent executes a discrete action  $a \in \{0, \dots, 8\}$ ,

$$\Delta \mathbf{x} = \begin{cases} \mathbf{0}, & a = 0, \\ v_m \mathbf{d}_a, & 1 \leq a \leq 8, \end{cases} \quad (11)$$

where  $\{\mathbf{d}_a\}$  are the eight unit directions. The observation stacks features of the four nearest obstacles:

$$\mathbf{o} = [o_1^\top, o_2^\top, o_3^\top, o_4^\top]^\top \in \mathbb{R}^{16}, \quad (12)$$

$$o_i = \left[ \frac{\Delta x_i}{D_{\max}}, \frac{\Delta y_i}{D_{\max}}, \frac{v_{x,i}}{v_{c,\max}}, \frac{v_{y,i}}{v_{c,\max}} \right]^\top, \quad D_{\max} = \sqrt{W^2 + H^2}. \quad (13)$$

If fewer than four obstacles exist, zero padding fills the remaining slots.

**Reward shaping and regimes.** Let the potential be the minimum signed clearance to any safety zone,

$$\phi_t = \min_i \left( \|\mathbf{m}_t - \mathbf{c}_{i,t}\| - r_i^{\text{sim}} \right). \quad (14)$$

While  $\phi_t \geq 0$  (outside all safety zones), the microrobot continues in its chosen direction and receives no reward. When  $\phi_t < 0$ , the learned policy acts, and the step reward is

$$r_t = k_{\text{shape}}(\phi_t - \phi_{t-1}) - \delta_t.$$

**Table 1: Simulation environment parameters.**

Parameter (Symbol)	Value
Arena dimensions ( $W \times H$ )	2000 $px \times$ 2000 $px$
Microrobot radius ( $R$ )	25 $px$
Microrobot speed ( $v_m$ )	10 $px/step$
Dynamic obstacles ( $N_d$ )	50
Static obstacles ( $N_s$ )	5
Obstacle radius ( $r_i$ )	[25, 50] $px$
Obstacle speed ( $v_i$ )	[4, 8] $px/step$
Time step ( $\Delta$ )	0.04 $s$

**Table 2: Reward function hyperparameters.**

Parameter (Symbol)	Value
Shaping reward weight ( $k_{\text{shape}}$ )	1.0
Time penalty ( $\delta_t$ )	0.05
Collision penalty ( $R_{\text{collision}}$ )	-50
Success reward ( $R_{\text{success}}$ )	50

A collision ends the episode with penalty  $R_{\text{collision}}$  when  $\|\mathbf{m}_t - \mathbf{c}_{i,t}\| < r_i + R$ . The first exit from all safety zones yields a bonus  $R_{\text{success}}$ . The full reward is

$$r_t = \begin{cases} k_{\text{shape}}(\phi_t - \phi_{t-1}) - \delta_t, & \phi_t < 0, \\ R_{\text{collision}}, & \|\mathbf{m}_t - \mathbf{c}_{i,t}\| < r_i + R, \\ R_{\text{success}}, & \phi_{t-1} < 0 \wedge \phi_t \geq 0, \\ 0, & \phi_t \geq 0. \end{cases} \quad (15)$$

Tables 1 and 2 list environment and reward parameters.

**Training.** We use eight parallel environment workers with an episode-level monitor. Transitions are stored in a replay buffer of size 500,000; each update samples a minibatch of 256. After 5,000 warm-up steps, the learner updates every 4 environment steps and syncs a target network every

1,000 steps. The discount factor is 0.99.  $\varepsilon$  decays linearly from 1 to 0.01 over the first 40% of training. The learning rate decays linearly from  $10^{-4}$  to 0.

We approximate the optimal action-value function with  $Q_\theta$  and a periodically synchronized target  $Q_{\bar{\theta}}$ . The Bellman equation is

$$Q^*(s_t, a_t) = \mathbb{E} \left[ r_t + \gamma \max_{a'} Q^*(s_{t+1}, a') \right]. \quad (16)$$

Given minibatches  $(s_t, a_t, r_t, s_{t+1}, d_{t+1})$  with  $d_{t+1} \in \{0, 1\}$ , the one-step target is

$$y_t = r_t + \gamma(1 - d_{t+1}) \max_{a'} Q_{\bar{\theta}}(s_{t+1}, a'). \quad (17)$$

We minimize the Huber loss

$$\mathcal{L}(\theta) = \mathbb{E} \left[ \rho_\kappa(y_t - Q_\theta(s_t, a_t)) \right], \quad \kappa = 1, \quad (18)$$

with stop-gradient on  $Q_{\bar{\theta}}$ .

**Evaluation.** Every 5,000 gradient updates, training pauses for 50 validation episodes in a separate instance, logging average return, length, and success rate. A random-policy baseline (uniform over actions) achieves a 50% success rate and mean return  $-1.13$ . When success improves over the best so far (ties by higher return), we snapshot the policy. Training stops after  $10^6$  environment steps in total, and the final policy is saved. Table S2 summarize all DQN training hyperparameters. Algorithm 5 describes the DQN training with global–local switch for dynamic obstacle avoidance.

**Outcomes.** Figure 5(B) shows learning curves. The smoothed episode return rises from near zero to about 25–30 and stabilizes. The success rate increases from roughly 50% to an average of 70–80%, with peaks near 90%. Figure 5(C) and Movie S4 show a simulated sequence. Unlike fixed hand-crafted rules, the RL-based controller adapts to the current obstacle configuration, often producing shorter detours and smoother trajectories. When the global plan is temporarily infeasible, the controller holds position rather than colliding (frames 135–165). Overall, the learned policy reliably avoids moving obstacles in cluttered scenes.

## Simulation Results of Local Escape Controllers

In a dynamic environment, the global planner (AGP) replans a collision-free path in real-time from the current microrobot, obstacle, and target states. The microrobot tracks the first waypoint on the

current plan. We evaluate performance with and without local escape controllers (rule-based and RL-based) under three scenarios that share the same dynamics.

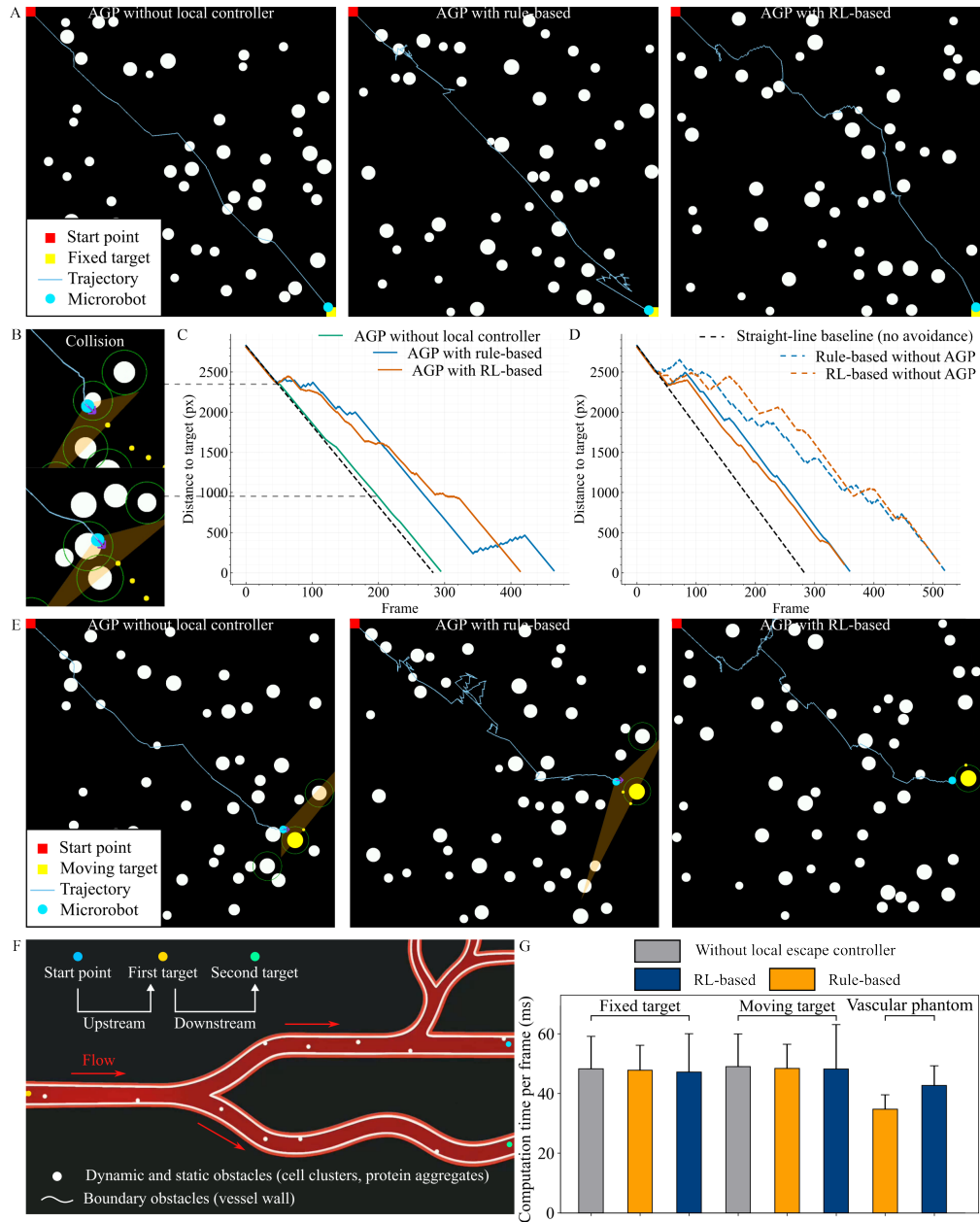
We use a  $2000 \times 2000$  px arena with 50 dynamic and 5 static obstacles (radii 25–50 px). Dynamic obstacles move at 4–8 px/frame along one of 16 evenly spaced directions from  $0^\circ$ – $360^\circ$ , undergoing elastic collisions with walls and other obstacles. The microrobot has radius 25 px and speed 10 px/frame. For AGP, we set  $\alpha = 6$ .

Figure 6(A) places the start in the upper-left corner and a fixed target in the lower-right corner. With AGP alone, the microrobot follows the global path but occasionally collides with fast nearby obstacles whose motion is not aligned with the microrobot’s direction (collisions illustrated in 6(B)). Figure 6(C) plots distance to target versus frame for the three methods in Figure 6(A), including a straight-line baseline (no global planner and no local controller; the microrobot drives directly toward the target at constant speed). Coupling AGP with either a local controller eliminates collisions and reaches the target. The RL-based controller shows the steepest, smoothest descent (fewer plateaus), indicating shorter detours and fewer stops. The rule-based controller also converges reliably but exhibits short plateaus when intermediate symmetric waypoints are triggered. Additional cluttered scenes with circular and rectangular obstacles using AGP with local controllers can be found in Figure S9 and Movie S5.

Figure 6(E) repeats the test with a moving target. Without a local controller, multiple collisions occur. With either local controller, the microrobot arrives without collision. The controllers exhibit distinct styles: the rule-based controller generates symmetric intermediate waypoints and may produce back-and-forth motion, whereas the RL-based controller reacts to observed obstacle positions and velocities to produce smoother, shorter detours.

Figure 6(F) models a vessel with boundary obstacles (walls) and circular static and dynamic obstacles (radius 10 px) that mimic cell clusters or protein aggregates. The boundary safety zone is formed by discretizing the wall contour into a grid of width 30 px. Flow proceeds from left to right. The microrobot (radius 8 px) moves upstream from the upper-right branch to a first target (yellow) at 3 px/frame, then downstream to a second target (green) at 5 px/frame. With AGP plus either local controller, the microrobot reaches both targets while avoiding static and dynamic obstacles.

Figure 6(G) reports computation time per frame across all three scenarios, with and without local controllers. In every case, the time remains below 50 ms, and adding a local controller does not



**Figure 6: Simulation results for dynamic obstacle avoidance (see Movie S5).** (A) Fixed target: trajectories under the three methods. (B) Collisions observed in AGP without local controllers. (C) Distance to target for the three methods in (A). (D) Distance to target with and without AGP. (E) Moving target: trajectories under the three methods. (F) Vascular phantom with boundary obstacles and static/dynamic circular obstacles; upstream and downstream segments between two fixed targets. (G) Computation time per frame for all scenarios and methods; all remain below 50 ms.

increase the per-frame budget. The hybrid system, therefore, meets real-time requirements while preserving reliability and robustness in complex dynamic scenes.

To evaluate the role of AGP in dynamic obstacle avoidance, we compare each local controller run alone (no global planner) against the same controller coupled with the AGP global planner. Figure S10 and Movie S6 show the comparison results in simulation. Figure 6(D) compares distance to target traces with and without AGP in Figure S10(B). Running only a local controller without AGP yields slower progress with long plateaus, frequent detours, and occasional collisions or getting stuck. Coupling either local controller with AGP restores a steady, largely monotonic decrease and reaches the goal sooner, showing that AGP provides essential long-range guidance while the local controllers handle short-range interactions.

## Experimental validation

We validated the framework in a range of benchtop settings. Figure 7(A) shows AGP in a static scene with a magnetic microrobot of radius  $20\ \mu\text{m}$  and multiple  $20\ \mu\text{m}$  silica particles. The red curve is the AGP solution path; the blue curve is the microrobot's actual trajectory under closed-loop control. Microrobot actuation and closed-loop control can be found in Supplementary Text. We repeated the test with a  $4.3\ \mu\text{m}$  microrobot navigating among Chinese hamster ovary (CHO) cells (Figure 7(B)). In both cases, the operator selected the microrobot and a target; AGP produced a collision-free path, and the microrobot autonomously followed it to the goal. Across multiple trials with varied silica particles and cell layouts, the microrobot reached the target without collisions (see Figure S5(B),(C), and Movie S1).

To stress real-time planning, a new AGP path was recomputed on every video frame from the current microrobot, obstacle, and target states, and the microrobot tracked the first waypoint. The simulation of AGP without local controller can be found in Figure S6, Figure S7, and Movie S2. The simulation results demonstrate the initial capability of real-time AGP to avoid slow-moving obstacles. Figure 7(C), Figure S8, and Movie S3 show a  $10\ \mu\text{m}$  microrobot navigating among CHO cells by real-time AGP; the trajectory maintains clearance from nearby cells. Figure 7(D) and Movie S3 show a  $20\ \mu\text{m}$  microrobot in a microfluidic channel  $200\ \mu\text{m}$  wide (no flow), again demonstrating safe real-time guidance.

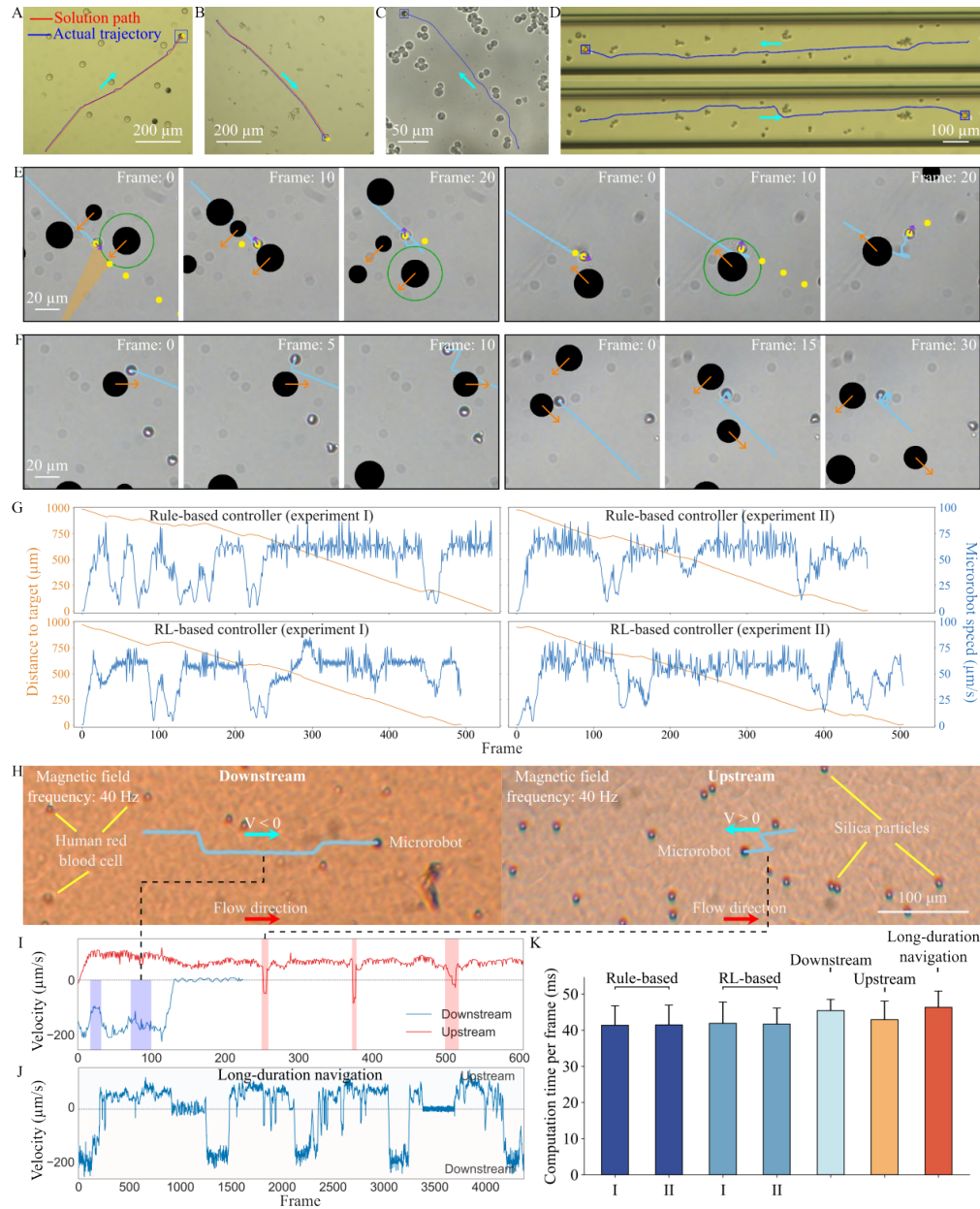


**Figure 7: Experimental validation of the planning and avoidance framework. (A)** AGP in a static scene with silica particles. **(B)** AGP with CHO cells **(C)** Real-time AGP: microrobot navigating among CHO cells. **(D)** Real-time AGP in a microfluidic channel with CHO cells (no flow). **(E)** Rule-based controller: two representative obstacle-avoidance sequences. **(F)** RL-based controller: four representative sequences. **(G)** Distance to target and microrobot speed during dynamic avoidance. **(H)** Flowing environment: downstream and upstream demonstrations. **(I)** Velocity traces: downstream and upstream. **(J)** A long-duration trial with repeated transits. **(K)** Computation time per frame across scenarios.

To stress real-time planning, AGP was recomputed at every video frame from the current microrobot, obstacle, and target states, and the microrobot tracked the first waypoint of the current plan. Simulations with AGP alone (no local controller) are shown in Figure S6, Figure S7, and Movie S2, which demonstrate that real-time AGP has the initial capability to avoid slow-moving obstacles. In experiments, a  $10\ \mu\text{m}$  microrobot navigated among CHO cells under real-time AGP while maintaining clearance from nearby cells (Figure 7(C), Figure S8, MovieS3). A  $20\ \mu\text{m}$  microrobot in a  $200\ \mu\text{m}$  wide microfluidic channel (no flow) was guided safely to the target (Figure 7(D), Movie S3).

We next combined AGP with the local controllers. A  $10\ \mu\text{m}$  microrobot was observed under a  $10\times$  objective; the rotating magnetic field was 35 Hz. Black circular objects served as dynamic obstacles. AGP updated the path every frame. When an obstacle approached within a threshold, control switched to a local controller. Both the rule-based and RL-based controllers guided the microrobot to the goal without collisions (See Movie S7). Figure 7(E) illustrates two avoidance sequences for the rule-based controller and Figure 7(F) shows four for the RL-based controller. Figure 7(G) plots the distance to target and microrobot speed (estimated from a 15-frame window to reduce noise). Sharp speed changes and small non-monotonicities in distance correspond to avoidance maneuvers. The average speed in these trials was approximately  $65\ \mu\text{m s}^{-1}$ .

To test generalization, we evaluated in a flowing microfluidic channel (Figure 7(H) and Movie S9). The rule-based controller is less efficient here: with unidirectional flow, symmetric reflections can induce backward motion when the arrow tip enters a safety zone. Without any retraining for flow, the RL-based controller generalized better. For upstream demonstrations we used a  $10\ \mu\text{m}$  microrobot and  $10\ \mu\text{m}$  silica particles mixed with red dye; for downstream we used a  $10\ \mu\text{m}$  microrobot in diluted human red blood cells with dye. The mean flow speed was  $\approx 400\ \mu\text{m s}^{-1}$  and the magnetic field was 40 Hz. Figure 7(I) shows velocity traces: downstream  $V < 0$  and upstream  $V > 0$ . The shaded intervals correspond to the avoidance during the navigation. The measured mean microrobot speeds were  $\sim 164\ \mu\text{m s}^{-1}$  downstream and  $\sim 62\ \mu\text{m s}^{-1}$  upstream. A long-duration trial (see Movie S10) with repeated upstream and downstream transits produced periodic speed profiles (Figure 7(J)). Throughout the run, the microrobot reached multiple sequential targets in both directions while navigating through flowing human red blood cells. All arrivals were collision-free, demonstrating stable, reliable operation over extended durations.

Across all scenarios, the per-frame computation time was less than 50 ms (Figure 7(K)), confirming real-time operation for dynamic avoidance.

## DISCUSSION

This work demonstrates a modular navigation framework that couples an analytic-geometry global planner (AGP) with two complementary local escape controllers (rule-based and RL-based). Across six families of static environments, AGP produced shorter paths and lower planning times than weighted A\*, PSO, and RRT, while remaining deterministic. In dynamic scenes, the local controllers handled short-range interactions with moving obstacles and maintained collision-free motion. End-to-end processing remained within a real-time budget (total computation < 50 ms per frame), matching typical microscopy frame rates and enabling closed-loop control. Benchtop experiments with silica particles, CHO cells, and flowing suspensions further showed that the hybrid planner executes reliable avoidance and that the RL-based controller generalizes better than hand-crafted rules when flow imposes strong directional bias.

**Significance.** The key advantage of AGP is that it avoids exhaustive search and random sampling, which reduces variance and makes timing short. Deterministic path construction and explicit safety zones also aid verification and controller handoff. Restricting learning to a local, short-range policy improves sample efficiency and isolates failures: global plans remain interpretable and can be replanned at video rate, while the learned controller only intervenes within well-defined neighborhoods. Together, these properties move microrobot navigation toward practical autonomy in cluttered vascular-like environments and provide a template for combining certifiable global planning with reactive, data-driven behaviors.

**Limitations.** First, the system relies on accurate image segmentation and tracking. Missed or fragmented masks, latency in the perception pipeline, or occlusions can shrink the true safety margin and cause avoidable interventions or collisions. Second, performance depends on imaging quality and frame rate. In vivo, modality-specific constraints (for example, penetration depth, field of view, and signal-to-noise ratio) will limit the usable control bandwidth. Third, our three-dimensional extension selects an optimal cross-sectional plane and lifts the path back to 3D, which preserves speed but does not yet achieve a fully 3D time-varying path.

**Future directions.** Two lines of work are especially promising. On the perception side, learned segmentation and tracking tailored to microscopic imagery could increase robustness and reduce latency. Self-supervised or weakly supervised models (for example, U-Net or transformer variants adapted to bright-field and fluorescence) combined with multi-object tracking would provide more reliable obstacle states and uncertainty estimates. On the planning and control side, extending the framework to fully 3D, time-varying scenes where obstacles flow with the fluid and interact across planes will be crucial for in vivo applications of microrobots.

Additional opportunities include hardware acceleration for instrumentation deployment, and closed-loop learning that adapts  $\alpha$  and safety zone inflation online. Beyond single-agent navigation, coordinating multiple microrobots with collision avoidance and task allocation may leverage AGP's determinism for global planning while keeping local interactions learned and reactive.

In summary, the presented hybrid framework delivers fast, deterministic global planning and effective local avoidance at video rate, a combination that is essential for safe operation in dense, dynamic microenvironments. Addressing perception reliability and extending the method to truly 3D dynamic scenes are the main steps toward in vivo navigation, where robust imaging and real-time autonomy will be coequal requirements.

## MATERIALS AND METHODS

### Experimental Setup

Figure 8(A) and Figure S11 show the benchtop platform. A microfluidic chip with four straight channels (width  $1000\ \mu\text{m}$ , depth  $200\ \mu\text{m}$ ) is connected via silicone tubing and Luer fittings to two programmable syringe pumps. Pump A continuously infuses the working fluid, and Pump B withdraws at the same rate, establishing a controlled, steady flow. The chip is centered within a three-axis Helmholtz coil set mounted on a Zeiss Axiovert 200M inverted microscope with a  $4\times$  objective for real-time optical observation. The coil system comprises three orthogonal Helmholtz pairs with different dimensions wound from copper wire; detailed parameters are provided in Table S3. Compared with quadrupole magnetic tweezers (20), the Helmholtz configuration offers a larger homogeneous workspace, which facilitates experimental validation of our navigation framework.

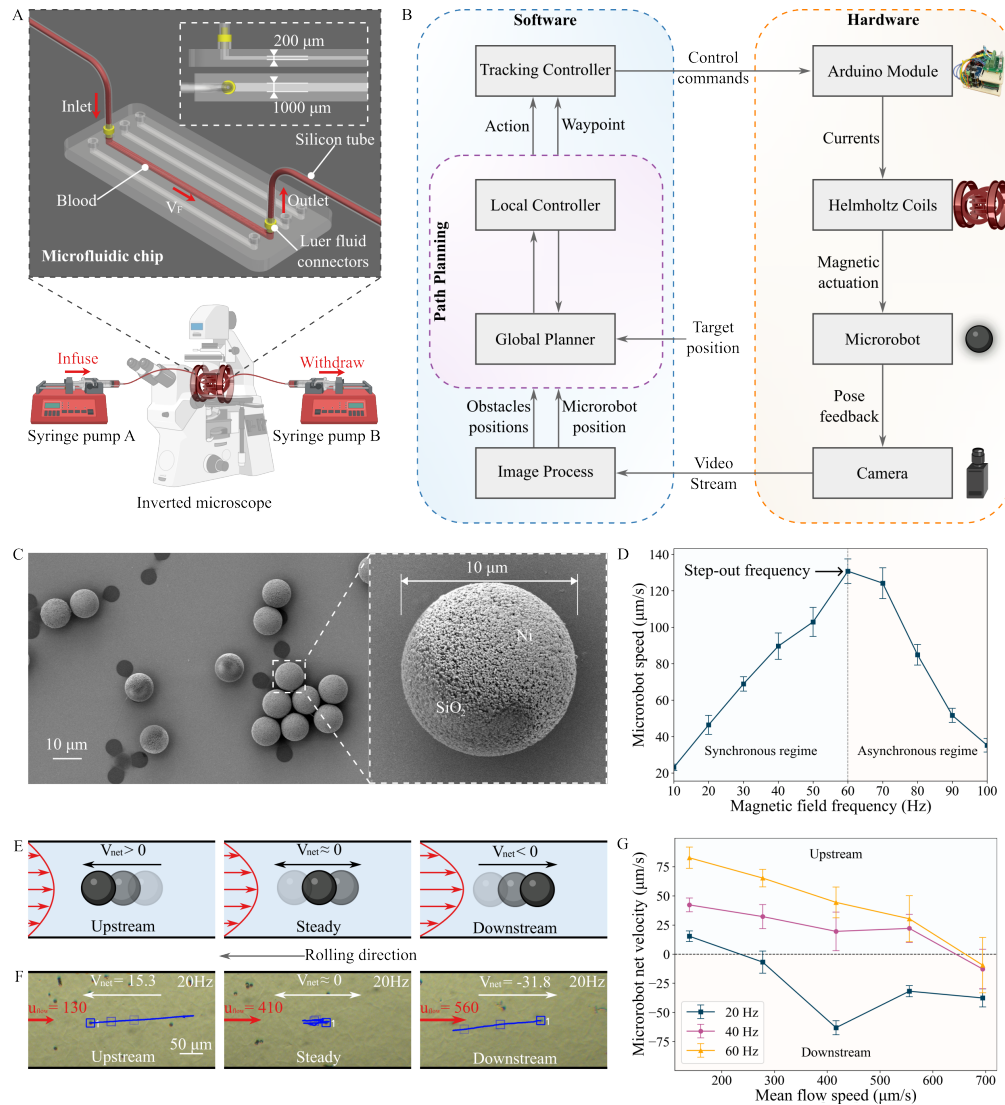


**Figure 8: Experimental setup and performance characterization.** (A) Microfluidic platform: straight channel connected to two syringe pumps that establish controlled flow; the chip sits within a three-axis Helmholtz coil set on an inverted microscope. (B) Closed-loop software hardware architecture (C) SEM of a 10  $\mu\text{m}$   $\text{SiO}_2$  bead with a Ni half shell. (D) Rolling speed versus rotating field frequency showing synchronous and asynchronous regimes. (E) Schematic of upstream, steady, and downstream regimes under flow. (F) Bright-field snapshots at 20 Hz with measured  $V_{\text{net}}$  and mean flow speed  $u_{\text{flow}}$ . (G) Mean net velocity  $V_{\text{net}}$  versus mean flow speed  $u_{\text{flow}}$  at  $f = 20, 40, \text{ and } 60$  Hz.

Figure 8(B) outlines the architecture integrating imaging, planning, and actuation. A high-speed FLIR BFS-U3-50S5C-C camera streams video to the tracking and planning software. Each frame is processed to estimate the microrobot pose and obstacle positions; the global planner produces waypoints, and the local controller computes low-level actions. A tracking controller converts actions to serial commands for an Arduino Mega 2560 with H-bridge drivers and a DC power supply. The drivers deliver current to the Helmholtz coils to generate the control fields. Camera-based pose feedback closes the loop in real-time, enabling adaptive trajectory updates and precise magnetic steering.

Magnetic microspheres were fabricated by coating commercial  $10\ \mu\text{m}$   $\text{SiO}_2$  beads (Spherotech) with a half-shell of Ni using electron-beam physical vapor deposition. The SEM image in Figure 8(C) shows a uniform Ni film covering approximately one hemisphere of each silica core. Figure 8(D) reports rolling speed versus rotating-field frequency inside the channels. In the synchronous regime (below  $\sim 60$  Hz), speed increases nearly linearly with frequency, reaching  $\approx 130\ \mu\text{m s}^{-1}$ . At the step-out frequency, the microrobot fails to follow the field and enters an asynchronous regime with a steep drop in speed.

Figures 8(E–G) and Movie S8 characterize transitions between upstream, steady, and downstream motion under constant frequency actuation. In Figure 8(E) we schematize three regimes for the microrobot driven by the rotating field: (i) upstream when its wall-coupled rolling speed exceeds the background flow ( $v_{\text{roll}} > u_{\text{flow}}$ , hence  $V_{\text{net}} > 0$ ); (ii) steady when  $v_{\text{roll}} \approx u_{\text{flow}}$  and  $V_{\text{net}} \approx 0$ ; and (iii) downstream when  $u_{\text{flow}} > v_{\text{roll}}$  and  $V_{\text{net}} < 0$ . Bright-field snapshots at 20 Hz for each regime appear in Figure 8(F) with measured  $V_{\text{net}}$  and  $u_{\text{flow}}$ . Quantitatively,

$$V_{\text{net}} = v_{\text{roll}} - u_{\text{flow}}, \quad v_{\text{roll}} = \alpha (2\pi R f), \quad (19)$$

where  $R$  is microrobot radius,  $f$  the rotation frequency, and  $\alpha$  a dimensionless wall-coupling coefficient ( $\alpha < 1$  accounts for hydrodynamic slip and imperfect rolling contact). Figure 8(G) plots mean  $V_{\text{net}}$  versus  $u_{\text{flow}}$  (taken here as the mean flow speed in the channel) for  $f = 20, 40,$  and  $60$  Hz:  $V_{\text{net}}$  is positive for  $u_{\text{flow}} < v_{\text{roll}}$ , crosses zero near  $u_{\text{flow}} \approx v_{\text{roll}}$ , and becomes negative at higher flows.

## **Computational Environment**

Simulations were run on a MacBook with an Apple M3 Pro (12 CPU cores, 18 GB unified memory). Experiments were executed on a 64-bit Windows workstation with an Intel Core i7-9700K (3.60 GHz) and 16 GB RAM. Algorithms were implemented in Python 3.10. Contour detection and visualization used OpenCV; computation times were measured with `time.time()` for high-resolution timing. Reinforcement learning experiments were conducted in Python 3.10 using Gymnasium for environment simulation and Stable-Baselines3 (DQN) for training.

## **Blood Preparation and Cell Culture**

Whole blood was obtained from STEMCELL Technologies (catalog 70508.2; donor RB1910; acquired 20 March 2025). Cells were diluted 1:40 in Dulbecco's phosphate-buffered saline (DPBS; Gibco, 14040133) by directly diluting whole blood with DPBS.

All cell culture reagents were from Gibco (BenchStable, USA). Chinese hamster ovary (CHO) cells were provided by collaborators. Cells were maintained in DMEM/F-12 supplemented with 10 % fetal bovine serum (FBS) and 1 % penicillin–streptomycin under standard culture conditions. When cultures reached approximately 85 % confluence, cells were washed with DPBS and detached using TrypLE Express (Gibco). Cells between passages 3–8 were used.

## References and Notes

1. B. J. Nelson, S. Pané, Delivering drugs with microrobots. *Science* **382** (6675), 1120–1122 (2023).
2. C. K. Schmidt, M. Medina-Sánchez, R. J. Edmondson, O. G. Schmidt, Engineering microrobots for targeted cancer therapies from a medical perspective. *Nature Communications* **11** (1), 5618 (2020).
3. M. T. Manzari, *et al.*, Targeted drug delivery strategies for precision medicines. *Nature Reviews Materials* **6** (4), 351–370 (2021).
4. M. Sitti, *et al.*, Biomedical applications of untethered mobile milli/microrobots. *Proceedings of the IEEE* **103** (2), 205–224 (2015).
5. B. Ahmad, M. Gauthier, G. J. Laurent, A. Bolopion, Mobile microrobots for in vitro biomedical applications: A survey. *IEEE Transactions on Robotics* **38** (1), 646–663 (2021).
6. X. Ju, *et al.*, Technology Roadmap of Micro/Nanorobots. *ACS nano* (2025).
7. B. J. Nelson, I. K. Kaliakatsos, J. J. Abbott, Microrobots for minimally invasive medicine. *Annual review of biomedical engineering* **12**, 55–85 (2010).
8. M. Sitti, Voyage of the microrobots. *Nature* **458** (7242), 1121–1122 (2009).
9. J. Li, *et al.*, Development of a magnetic microrobot for carrying and delivering targeted cells. *Science robotics* **3** (19), eaat8829 (2018).
10. S. Das, *et al.*, Boundaries can steer active Janus spheres. *Nature communications* **6** (1), 8999 (2015).
11. L. Yang, *et al.*, A survey on swarm microrobotics. *IEEE Transactions on Robotics* **38** (3), 1531–1551 (2021).
12. L. E. Beaver, *et al.*, Closed-loop Control for a Heterogeneous Group of Magnetically-actuated Microrobots, in *2023 International Conference on Manipulation, Automation and Robotics at Small Scales (MARSS)* (IEEE) (2023), pp. 1–6.

13. M. Sokolich, D. Rivas, Y. Yang, M. Duey, S. Das, ModMag: A modular magnetic micro-robotic manipulation device. *MethodsX* **10**, 102171 (2023).
14. Y. Yang, D. Rivas, M. Sokolich, S. Das, Closed-Loop Control of Bubble-Propelled Microrobots, in *2023 International Conference on Manipulation, Automation and Robotics at Small Scales (MARSS)* (IEEE) (2023), pp. 1–6.
15. A. Ozcelik, *et al.*, Acoustic tweezers for the life sciences. *Nature methods* **15** (12), 1021–1028 (2018).
16. S. Das, *et al.*, Controlled delivery of signaling molecules using magnetic microrobots, in *2018 international conference on manipulation, automation and robotics at small scales (MARSS)* (IEEE) (2018), pp. 1–5.
17. M. E. Tiryaki, F. Doğangün, C. B. Dayan, P. Wrede, M. Sitti, MRI-powered Magnetic Miniature Capsule Robot with HIFU-controlled On-demand Drug Delivery, in *2023 IEEE International Conference on Robotics and Automation (ICRA)* (IEEE) (2023), pp. 5420–5425.
18. M. Sokolich, S. Mallick, Z. H. Shah, Y. Yang, S. Das, Cellular cargo manipulation using magnetically steerable microrobots in dense environments, in *Proceedings of the 2023 6th International Conference on Advances in Robotics* (2023), pp. 1–5.
19. Y. Yang, *et al.*, Rolling Helical Microrobots for Cell Patterning, in *2023 International Conference on Manipulation, Automation and Robotics at Small Scales (MARSS)* (IEEE) (2023), pp. 1–6.
20. Y. Yang, M. Sokolich, S. Mallick, S. Das, Quadrupole Magnetic Tweezers for Precise Cell Transportation. *IEEE Transactions on Biomedical Engineering* (2024).
21. K. Meng, *et al.*, Motion planning and robust control for the endovascular navigation of a microrobot. *IEEE Transactions on Industrial Informatics* **16** (7), 4557–4566 (2019).
22. Q. Fan, G. Cui, Z. Zhao, J. Shen, Obstacle avoidance for microrobots in simulated vascular environment based on combined path planning. *IEEE Robotics and Automation Letters* **7** (4), 9794–9801 (2022).

23. Y. Yang, M. A. Bevan, B. Li, Hierarchical planning with deep reinforcement learning for 3D navigation of microrobots in blood vessels. *Advanced Intelligent Systems* **4** (11), 2200168 (2022).
24. Q. Wang, *et al.*, Ultrasound Doppler-guided real-time navigation of a magnetic microswarm for active endovascular delivery. *Science Advances* **7** (9), eabe5914 (2021).
25. S. A. Abbasi, *et al.*, Autonomous 3D positional control of a magnetic microrobot using reinforcement learning. *Nature Machine Intelligence* **6** (1), 92–105 (2024).
26. D. Wu, *et al.*, Femtosecond laser-assisted printing of hard magnetic microrobots for swimming upstream in subcentimeter-per-second blood flow. *Science Advances* **11** (27), eadw1272 (2025).
27. L. Yang, Y. Zhang, Q. Wang, K.-F. Chan, L. Zhang, Automated control of magnetic spore-based microrobot using fluorescence imaging for targeted delivery with cellular resolution. *IEEE Transactions on Automation Science and Engineering* **17** (1), 490–501 (2019).
28. Q. Wang, L. Yang, L. Zhang, Micromanipulation using reconfigurable self-assembled magnetic droplets with needle guidance. *IEEE Transactions on Automation Science and Engineering* **19** (2), 759–771 (2021).
29. Z. Yang, L. Yang, L. Zhang, Autonomous navigation of magnetic microrobots in a large workspace using mobile-coil system. *IEEE/ASME Transactions on Mechatronics* **26** (6), 3163–3174 (2021).
30. M. Li, L. Li, J. Zhou, L. Liu, N. Jiao, Deep learning-based automatic control of magnetic diatom biohybrid microrobots for targeted delivery. *IEEE Transactions on Robotics* (2025).
31. J. Liu, T. Xu, S. X. Yang, X. Wu, Navigation and visual feedback control for magnetically driven helical miniature swimmers. *IEEE Transactions on Industrial Informatics* **16** (1), 477–487 (2019).
32. M. Salehizadeh, E. D. Diller, Path planning and tracking for an underactuated two-microrobot system. *IEEE robotics and automation letters* **6** (2), 2674–2681 (2021).

33. L. Zheng, *et al.*, 3D navigation control of untethered magnetic microrobot in centimeter-scale workspace based on field-of-view tracking scheme. *IEEE Transactions on Robotics* **38** (3), 1583–1598 (2021).
34. Y. Liu, Z. Hou, J. Qu, X. Liu, Q. Fan, Optimized rrt planning with cma-es for autonomous navigation of magnetic microrobots in complex environments. *IEEE/ASME Transactions on Mechatronics* (2024).
35. J. Jiang, Z. Yang, A. Ferreira, L. Zhang, Control and autonomy of microrobots: Recent progress and perspective. *Advanced Intelligent Systems* **4** (5), 2100279 (2022).
36. T. Ye, T. Peng, L. Yang, Review on path planning for obstacle avoidance oriented to micro-/nanorobots. *Robot Learning* **1** (1), 1–23 (2024).
37. Y. Liu, *et al.*, Automatic navigation of microswarms for dynamic obstacle avoidance. *IEEE Transactions on Robotics* **39** (4), 2770–2785 (2023).
38. Y. Liu, *et al.*, Radar-Based Control of a Helical Microswimmer in 3-Dimensional Space with Dynamic Obstacles. *Cyborg and Bionic Systems* **6**, 0158 (2025).
39. H. Kim, U. K. Cheang, M. J. Kim, Autonomous dynamic obstacle avoidance for bacteria-powered microrobots (BPMs) with modified vector field histogram. *PloS one* **12** (10), e0185744 (2017).
40. T. Li, *et al.*, Autonomous collision-free navigation of microvehicles in complex and dynamically changing environments. *Acs Nano* **11** (9), 9268–9275 (2017).
41. J. Jiang, L. Yang, L. Zhang, DQN-based on-line path planning method for automatic navigation of miniature robots, in *2023 IEEE International Conference on Robotics and Automation (ICRA)* (IEEE) (2023), pp. 5407–5413.
42. L. Yang, *et al.*, Autonomous environment-adaptive microrobot swarm navigation enabled by deep learning-based real-time distribution planning. *Nature Machine Intelligence* **4** (5), 480–493 (2022).

43. G. Li, W. Chou, Path planning for mobile robot using self-adaptive learning particle swarm optimization. *Science China Information Sciences* **61**, 1–18 (2018).
44. M. Clerc, J. Kennedy, The particle swarm-explosion, stability, and convergence in a multi-dimensional complex space. *IEEE transactions on Evolutionary Computation* **6** (1), 58–73 (2002).

## Acknowledgments

AI-assisted tools (ChatGPT5, OpenAI) were used to improve grammar and clarity during manuscript preparation. The authors reviewed and take full responsibility for the final content.

**Funding:** The work of Andreas A. Malikopoulos was supported in part by the National Science Foundation under Grants CNS-2401007, CMMI-2348381, IIS-2415478, and in part by MathWorks. This work of Sambaeta Das was supported by the National Science Foundation under grant GCR 2219101, CPS 2234869, EFMA 2422282 and the National Health Institute under grant 1R35GM147451.

**Author contributions:** Y.Y. and A.M. conceived and designed the study. Y.Y. developed the algorithmic framework, implemented simulations, and performed the experiments. M.S. contributed to software implementation. F.C.K. prepared blood samples and maintained cell cultures. Y.Y. and S.D. wrote the manuscript with input from all authors. All authors reviewed and approved the final manuscript.

**Competing interests:** There are no competing interests to declare.

**Data and materials availability:** All data supporting the findings of this study are available in the paper and its Supplementary Materials. Raw microscopy videos and primary datasets are available from the corresponding author upon reasonable request.

## **Supplementary materials**

Supplementary Text

Figs. S1 to S11

Tables S1 to S3

Movie S1 to S10

Algorithm 1 to 5

**Supplementary Materials for**  
**Microrobot Vascular Parkour: Analytic Geometry–based Path**  
**Planning with Real-time Dynamic Obstacle Avoidance**

Yanda Yang, Max Sokolich, Fatma Ceren Kirmizitas, Sambaeta Das\*, Andreas A. Malikopoulos

\*Corresponding author. Email: [samdas@udel.edu](mailto:samd@udel.edu)

**This PDF file includes:**

Supplementary Text

Figures S1 to S11

Tables S1 to S3

Algorithm 1 to 5

Captions for Movies S1 to S10

**Other Supplementary Materials for this manuscript:**

Movies S1 to S10

## Supplementary Text

### Particle Swarm Optimization Implementation

Particle Swarm Optimization (PSO) is a population-based evolutionary method for stochastic optimization (43). We adapt the PSO path planning approach of (27). The goal is to choose  $K$  interior spline nodes so that a cubic spline (which interpolates  $\mathcal{S}$ , those  $K$  nodes, and  $\mathcal{E}$ ) yields a short, collision-free path when sampled at waypoints. The start  $\mathcal{S}$  and end  $\mathcal{E}$  are fixed. The  $x$ -coordinates of both the nodes and the waypoints are fixed and uniformly spaced between  $\mathcal{S}$  and  $\mathcal{E}$ . Let the waypoints be  $w_j = (x_{w,j}, y_{w,j})^\top$  for  $j = 1, \dots, J$ , and the obstacle centers  $c_i = (x_{c,i}, y_{c,i})^\top$  with safety zone radii  $r_i, i = 1, \dots, N$ .

To reduce compute time we evaluate path length on the  $J+1$  waypoints  $W = \{w_0, \dots, w_J\}$  with  $w_0 = \mathcal{S}$  and  $w_J = \mathcal{E}$ :

$$L(W) = \sum_{j=0}^{J-1} \|w_{j+1} - w_j\|_2. \quad (\text{S1})$$

We use a soft overlap penalty per waypoint

$$\phi_i(w_j) = \max \left\{ 1 - \frac{\|w_j - c_i\|_2}{r_i}, 0 \right\}, \quad (\text{S2})$$

and aggregate collisions as

$$V(W) = \sum_{i=1}^N \sum_{j=0}^J \phi_i(w_j). \quad (\text{S3})$$

The cost minimized by PSO is then

$$\text{Cost}(W) = L(W) (1 + C_v V(W)), \quad (\text{S4})$$

where  $C_v > 0$  is the collision penalty weight.

We optimize only the  $y$ -coordinates of the  $K$  interior spline nodes (node  $x$ -coordinates are fixed and uniformly spaced). Let  $P$  be the number of particles and  $G$  the number of iterations. Particle  $p$  at iteration  $g$  stores position  $\mathbf{y}_p^g \in \mathbb{R}^K$  (node ordinates) and velocity  $\mathbf{v}_p^g \in \mathbb{R}^K$ . Each particle tracks its personal best  $\mathbf{p}_p^b$  and the swarm tracks the global best  $\mathbf{g}^b$ . The velocity–position update is

$$\mathbf{v}_p^{g+1} = w \mathbf{v}_p^g + c_1 r_1 (\mathbf{p}_p^b - \mathbf{y}_p^g) + c_2 r_2 (\mathbf{g}^b - \mathbf{y}_p^g), \quad (\text{S5})$$

$$\mathbf{y}_p^{g+1} = \mathbf{y}_p^g + \mathbf{v}_p^{g+1}, \quad (\text{S6})$$

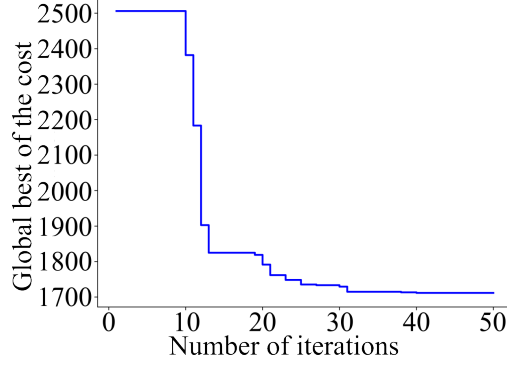


**Figure S1: Global best of the cost function in every iteration.**

with  $r_1, r_2 \sim \mathcal{U}[0, 1]$ , inertia  $w \in [0, 1]$ , and learning coefficients  $c_1, c_2 > 0$ . We use the Clerc–Kennedy constriction choice (44):

$$\chi = \frac{2k}{|2 - \phi - \sqrt{\phi^2 - 4\phi}|}, \quad k = 1, \quad \phi_1 = \phi_2 = 2.05, \quad w = \chi, \quad c_1 = \chi\phi_1, \quad c_2 = \chi\phi_2, \quad \phi = \phi_1 + \phi_2$$

which yields  $\chi \approx 0.729$ . We clamp  $\mathbf{v}_p^g \in [-v_{\max}, v_{\max}]^K$  and  $\mathbf{y}_p^g \in [y_{\min}, y_{\max}]^K$  each iteration. To accelerate convergence, the initial global best is the straight line between  $\mathcal{S}$  and  $\mathcal{E}$ . A damping factor  $w_{\text{damp}} \in (0, 1]$  gradually reduces  $w$ .

After optimization we evaluate the spline defined by the best node set to produce the  $J$  waypoints. Figure S1 plots the global best cost of the result in Figure 3(A). In the example,  $K = 5$  nodes and  $J = 25$  waypoints were sufficient to keep runtime modest. The microrobot and target are annotated in red and yellow, respectively.

---

**Algorithm 1** PSO-based obstacle avoidance

---

**Require:** start  $\mathcal{S}$ , end  $\mathcal{E}$ , interior nodes  $K$ , segments  $J$ , obstacles  $\{(c_i, r_i)\}_{i=1}^N$ ; PSO hyperparameters

$P, G, w, c_1, c_2, v_{\max}, y_{\min}, y_{\max}, w_{\text{damp}}$

- 1: Initialize the  $x$ -coordinates of the nodes uniformly from  $\mathcal{S}$  to  $\mathcal{E}$ ; set initial global best  $\mathbf{g}^b$  to the straight line
  - 2: Initialize particles  $\{\mathbf{y}_p^0, \mathbf{v}_p^0\}_{p=1}^P$  within  $[y_{\min}, y_{\max}]^K$ ; set  $\mathbf{p}_p^b \leftarrow \mathbf{y}_p^0$
  - 3: **for**  $g = 0$  to  $G - 1$  **do**
  - 4:     **for**  $p = 1$  to  $P$  **do**
  - 5:         Evaluate  $\text{Cost}(\mathbf{y}_p^g)$  by constructing the spline, sampling the  $J+1$  waypoints  $W$ , and computing  $L$  and  $V$
  - 6:         **if**  $\text{Cost}(\mathbf{y}_p^g) < \text{Cost}(\mathbf{p}_p^b)$  **then**  $\mathbf{p}_p^b \leftarrow \mathbf{y}_p^g$
  - 7:         **end if**
  - 8:         **if**  $\text{Cost}(\mathbf{p}_p^b) < \text{Cost}(\mathbf{g}^b)$  **then**  $\mathbf{g}^b \leftarrow \mathbf{p}_p^b$
  - 9:         **end if**
  - 10:         Sample  $r_1, r_2 \sim \mathcal{U}[0, 1]$
  - 11:         Update  $\mathbf{v}_p^{g+1} = w \mathbf{v}_p^g + c_1 r_1 (\mathbf{p}_p^b - \mathbf{y}_p^g) + c_2 r_2 (\mathbf{g}^b - \mathbf{y}_p^g)$ ; clamp to  $[-v_{\max}, v_{\max}]^K$
  - 12:         Update  $\mathbf{y}_p^{g+1} = \mathbf{y}_p^g + \mathbf{v}_p^{g+1}$ ; clamp to  $[y_{\min}, y_{\max}]^K$
  - 13:         **end for**
  - 14:      $w \leftarrow w \cdot w_{\text{damp}}$
  - 15:     **end for**
  - 16: **return** best interior node set  $\mathbf{g}^b$  and its sampled waypoints  $W$
- 

Swarming methods explore broadly and can escape local minima, but they incur non-trivial runtime and do not guarantee feasibility or optimality. Furthermore, the constraints are enforced indirectly via the penalty term and may be violated if  $\varepsilon$  is too small.

### Rapidly Exploring Random Tree Implementation

The rapidly exploring random tree (RRT) incrementally builds a tree rooted at the start  $\mathcal{S}$  by sampling the workspace and steering the tree toward each sample. Nodes represent feasible microrobot states in a 2D plane  $\Omega = [0, W] \times [0, H]$ .

At iteration  $k$ , a random point  $x_{\text{rand}} = (x_{\text{rand}}, y_{\text{rand}})^\top$  is drawn from  $\Omega$ . The nearest tree node is

$$x_{\text{near}} = \arg \min_{v \in T} \|v - x_{\text{rand}}\|_2.$$

A new candidate is generated by stepping a fixed distance  $\Delta s$  from  $x_{\text{near}}$  toward  $x_{\text{rand}}$ :

$$x_{\text{new}} = x_{\text{near}} + \Delta s \frac{x_{\text{rand}} - x_{\text{near}}}{\|x_{\text{rand}} - x_{\text{near}}\|_2}, \quad \theta = \text{atan2}(y_{\text{rand}} - y_{\text{near}}, x_{\text{rand}} - x_{\text{near}}). \quad (\text{S7})$$

The edge  $\overline{x_{\text{near}}x_{\text{new}}}$  is accepted if it is collision free with respect to every obstacle and  $x_{\text{new}}$  is added to the tree with parent  $x_{\text{near}}$ . The process repeats until  $\|x_{\text{new}} - \mathcal{E}\|_2 \leq \delta_{\text{tol}}$ , after which a final straight segment from  $x_{\text{new}}$  to  $\mathcal{E}$  is validated by the same check and the goal is attached. The path is recovered by backtracking parents from  $\mathcal{E}$  to  $\mathcal{S}$ .

RRT explores efficiently and is robust in cluttered scenes, but due to random sampling it produces variable paths across runs and offers no optimality guarantees.

### Weighted A\* Implementation

We employ weighted A\* (WA\*) to accelerate grid search. For a grid node  $n$ , the evaluation is

$$f(n) = g(n) + w h(n), \quad (\text{S8})$$

where  $g(n)$  is the accumulated cost from the start  $\mathcal{S}$ ,  $h(n)$  is a heuristic estimate from  $n$  to the goal  $\mathcal{E}$ , and  $w \geq 1$  weights the heuristic. The path cost is updated recursively: if  $m$  is the predecessor of  $n$ ,

$$g(n) = g(m) + c(m, n), \quad (\text{S9})$$

with 8 connected move costs

$$c(m, n) = \begin{cases} 1, & \text{horizontal/vertical,} \\ \sqrt{2}, & \text{diagonal.} \end{cases}$$

We use the Euclidean heuristic

$$h(n) = \sqrt{(x_e - x_n)^2 + (y_e - y_n)^2}. \quad (\text{S10})$$

To enforce collision avoidance with safety zones, a grid cell at center  $(x, y)$  is traversable only if, for every obstacle  $i$  with center  $c_i = (x_{c,i}, y_{c,i})^\top$  and radius of the safety zone  $r_i$ ,

$$[x - x_{c,i}]^2 + [y - y_{c,i}]^2 > r_i^2. \quad (\text{S11})$$

**Table S1: Hyperparameters used to generate Fig. S2(A).** Here  $\delta_{i,j}$  denotes the Kronecker delta (1 if  $i = j$ , else 0).

Path color	$\delta(i)$ (px)	Path length (px)
Pink (original)	0	3421.15
Red	$150 \delta_{i,1}$	3824.27
Blue	$50 \delta_{i,15}$	3665.68
Yellow	$100 \delta_{i,2} + 100 \delta_{i,6} + 200 \delta_{i,9}$	3749.68

WA\* expands the lowest- $f$  node from the open set, relaxes its 8 neighbors, and records backpointers. When  $\mathcal{E}$  is reached, the path is reconstructed by backtracking. WA\* consistently returns the same solution for a fixed grid and obstacle set. Larger  $w$  reduces runtime at the expense of optimality (with  $w = 1$ , WA\* simplifies to A\* and is optimal on this grid).

### Modification of the AGP solution path

Although AGP returns a unique path for a given frame, users may wish to increase clearance near specific obstacles or steer the trajectory through preferred regions. We introduce an obstacle inflation parameter  $\delta(i) \geq 0$  that enlarges the safety zone of obstacle  $i$  to

$$r'_i = r_i + \delta(i). \quad (\text{S12})$$

Here  $\delta(i)$  can be set selectively using the Kronecker delta  $\delta_{i,j}$  (equal to 1 when  $i = j$ , otherwise 0). For example,  $\delta(i) = 150 \delta_{i,1}$  inflates only obstacle 1 by 150 px. Figure S2(A) illustrates four paths generated by different  $\delta(i)$  choices. The pink curve is the original AGP solution ( $\delta(i) \equiv 0$ ), which is shortest (Table S1) but passes close to several cells and is therefore “riskier.” Inflating the first obstacle yields a more conservative red path at the cost of added length. Targeted inflations of obstacles  $\{2, 6, 9\}$  “push” the path into the yellow trajectory, which both crosses more cells and is longer. A localized change,  $\delta(i) = 50 \delta_{i,15}$ , produces the blue path: the first half matches the original, then diverges around obstacle 15.

This inflation against obstacles provides a simple, deterministic way to trade clearance for length without changing the environment or retuning the planner.

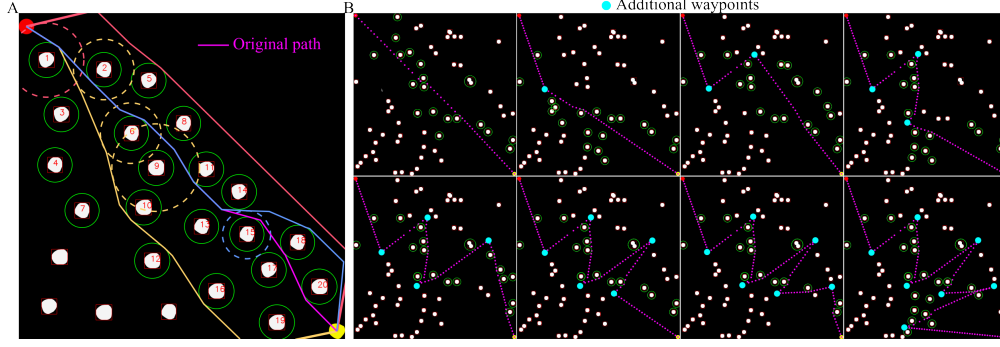


**Figure S2: Modifying AGP paths via safety zone inflation and user waypoints.** (A) Original AGP path (pink) compared with three modified paths generated by obstacle-specific radius inflation  $\delta(i)$ . (B) Sequential insertion of seven intermediate waypoints (blue) reshapes the route into a zigzag while preserving collision avoidance.

Beyond radius inflation, users can impose  $n$  additional intermediate waypoints

$$\{(\hat{x}_{w,1}, \hat{y}_{w,1}), \dots, (\hat{x}_{w,n}, \hat{y}_{w,n})\}$$

to shape the path. We run AGP sequentially from the start  $(x_s, y_s)$  to  $(\hat{x}_{w,1}, \hat{y}_{w,1})$ , then between consecutive waypoints, and finally from  $(\hat{x}_{w,n}, \hat{y}_{w,n})$  to the goal  $(x_e, y_e)$ . Connecting the segments yields the final trajectory. As shown in Figure S2(B), placing seven additional waypoints produces a zigzag path. Waypoints can be added interactively by clicking on the image, enabling rapid, operator-in-the-loop refinement.

### Microrobot actuation and closed-loop control

A rotating magnetic field produces a time-varying torque on the microrobot,

$$\boldsymbol{\tau}(t) = \mathbf{m} \times \mathbf{B}(t), \quad (\text{S13})$$

where  $\mathbf{m} \in \mathbb{R}^3$  is the magnetic moment. The field is synthesized by driving orthogonal Helmholtz pairs with sinusoids to create

$$\mathbf{B}(t) = \begin{bmatrix} B_x \\ B_y \\ B_z \end{bmatrix} = B_0 \begin{bmatrix} -\cos \beta \cos \alpha \cos \omega t + \sin \alpha \sin \omega t \\ -\cos \beta \sin \alpha \cos \omega t - \cos \alpha \sin \omega t \\ \sin \beta \cos \omega t \end{bmatrix}, \quad (\text{S14})$$

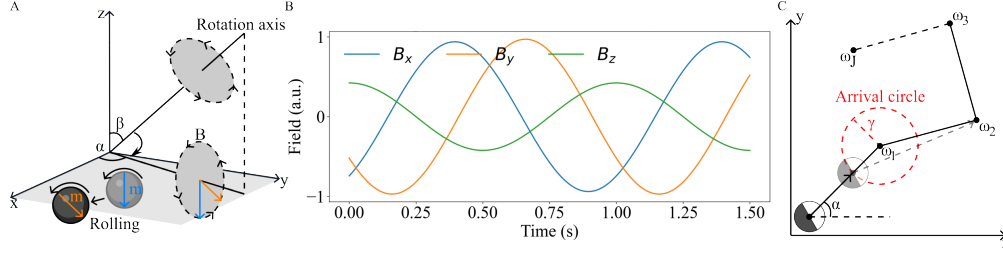


**Figure S3: Microrobot actuation and closed-loop control.** (A) Geometry of the rotating magnetic field: the rotation axis  $\hat{n}$  is parameterized by azimuth  $\alpha$  and tilt  $\beta$ ; the field vector  $\mathbf{B}(t)$  traces a circle in the plane orthogonal to  $\hat{n}$ . (B) Time traces of the normalized field components for  $\alpha = 35^\circ$ ,  $\beta = 25^\circ$ :  $B_z \propto \cos \omega t$ ;  $B_x$  and  $B_y$  are quadrature sinusoids whose amplitudes depend on  $\alpha$  and  $\beta$ . (C) Waypoint tracking in the plane: the “arrival circle” of radius  $\gamma$  defines the switch condition from waypoint  $\mathbf{w}_j$  to  $\mathbf{w}_{j+1}$ ; the azimuth  $\alpha$  is measured from the  $x$ -axis. In experiments we set  $\beta = \pi/2$  for planar rolling.

with amplitude  $B_0$ , angular frequency  $\omega$ , and fixed orientation angles  $\alpha$  and  $\beta$  (Figure S3(A)). In (S14),  $\alpha$  is the azimuth of the rotation axis in the  $xy$ -plane (from  $+x$  toward  $+y$ ), and  $\beta$  is the tilt of that axis away from  $+z$  (polar angle). The field magnitude is constant:  $\|\mathbf{B}(t)\| = \|\mathbf{B}\|$  for all  $t$ . The unit rotation axis is

$$\hat{n} = \begin{bmatrix} \cos \alpha \sin \beta \\ \sin \alpha \sin \beta \\ \cos \beta \end{bmatrix}.$$

For rolling on a planar substrate we set  $\beta = \frac{\pi}{2}$  so the rotation axis lies in the plane, which produces wall-coupled rolling. Figure S3(B) plots the normalized components of the rotating field for a representative setting ( $\alpha = 35^\circ$ ,  $\beta = 25^\circ$ ). As predicted by (S14),  $B_z$  follows  $\cos \omega t$  while  $B_x$  and  $B_y$  are quadrature sinusoids scaled by  $\alpha$ ,  $\beta$ . Varying  $\beta$  redistributes amplitude between the in-plane components ( $B_x$ ,  $B_y$ ) and the out-of-plane component ( $B_z$ ), whereas  $\alpha$  rotates the in-plane mixture of  $B_x$  and  $B_y$ . The three curves remain phase locked, reflecting a vector of constant magnitude that traces a circle orthogonal to the rotation axis.

Let the current microrobot position be  $\mathbf{m} = (x_m, y_m)^\top$  and the AGP waypoints  $W = \{\mathbf{w}_1, \dots, \mathbf{w}_J\}$ ,  $\mathbf{w}_j = (x_{w,j}, y_{w,j})^\top$  (Figure S3(C)). We steer by aligning the in-plane projection of  $\mathbf{B}(t)$  with the

bearing from  $\mathbf{m}$  to the active waypoint  $\mathbf{w}_j$ . Define the bearing and distance

$$\theta_j = \text{atan2}(y_{w,j} - y_m, x_{w,j} - x_m), \quad d_j = \|\mathbf{w}_j - \mathbf{m}\|.$$

The arrival circle has radius  $\gamma > 0$ . Algorithm 2 shows the control law.

---

**Algorithm 2** Closed-loop waypoint tracking with a rotating magnetic field

---

**Require:** Waypoints  $W = \{\mathbf{w}_1, \dots, \mathbf{w}_J\}$ , arrival radius  $\gamma$ , field amplitude  $B_0$ , frequency  $f = \omega/2\pi$

- 1: Set  $\beta \leftarrow \pi/2$  ▷ planar rolling
- 2:  $j \leftarrow 1$
- 3: **while**  $j \leq J$  **do**
- 4:     Measure microrobot position  $\mathbf{m} = (x_m, y_m)^\top$
- 5:      $d_j \leftarrow \|\mathbf{w}_j - \mathbf{m}\|$ ,    $\theta_j \leftarrow \text{atan2}(y_{w,j} - y_m, x_{w,j} - x_m)$
- 6:     **if**  $d_j \leq \gamma$  **then**
- 7:          $j \leftarrow j + 1$  ▷ advance to next waypoint
- 8:     **continue**
- 9:     **end if**
- 10:      $\alpha \leftarrow \theta_j + \pi/2$  ▷ azimuth of the rotation axis aligned to bearing
- 11:     Command field components (from (S14) with  $\beta = \pi/2$ ):

$$\mathbf{B}(t) = B_0 \begin{bmatrix} \sin \alpha \sin \omega t \\ -\cos \alpha \sin \omega t \\ \cos \omega t \end{bmatrix}$$

- 12: **end while**
-

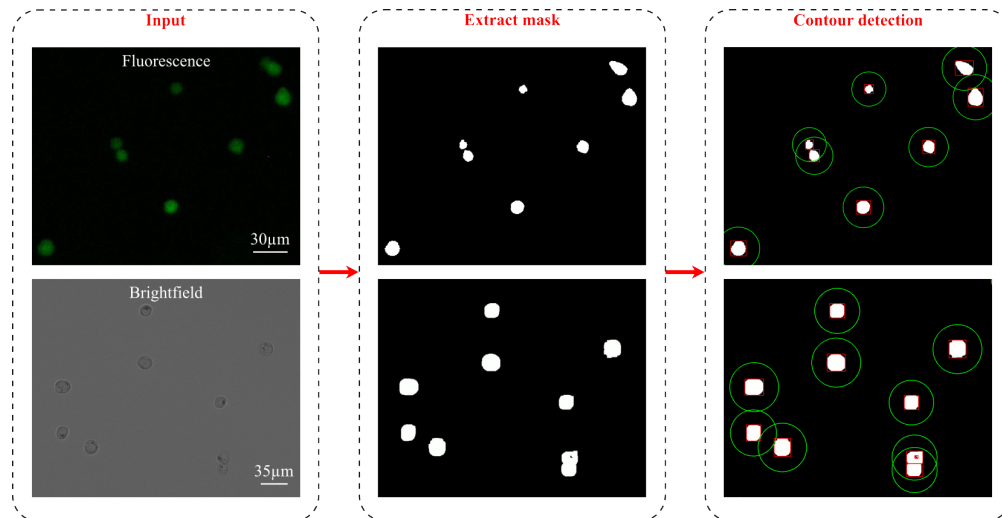


**Figure S4: Image processing pipeline for cell detection.** From left to right: raw inputs, binary masks extracted by thresholding, and contour detection with safety zones.

**Table S2: DQN training hyperparameters.**

Parameter (Symbol)	Value
Number of parallel environments $n_{\text{env}}$	8
Replay buffer capacity $N$	500 000
Batch size $B$	256
Initial exploration steps $S_{\text{ini}}$	5 000
Network update frequency $f$	4
Target-network update interval $K$	1 000
Discount factor $\gamma$	0.99
Initial exploration rate $\varepsilon_0$	1
Final exploration rate $\varepsilon_1$	0.01
$\varepsilon$ -annealing fraction $\alpha_\varepsilon$	40 %
Learning rate $\lambda_0$	$1 \times 10^{-4} \rightarrow 0$
Hidden layer sizes $\mathcal{A}$	[512, 256]
Evaluation frequency $F$	5 000
Evaluation episodes $M$	50
Total training steps $S$	$1 \times 10^6$

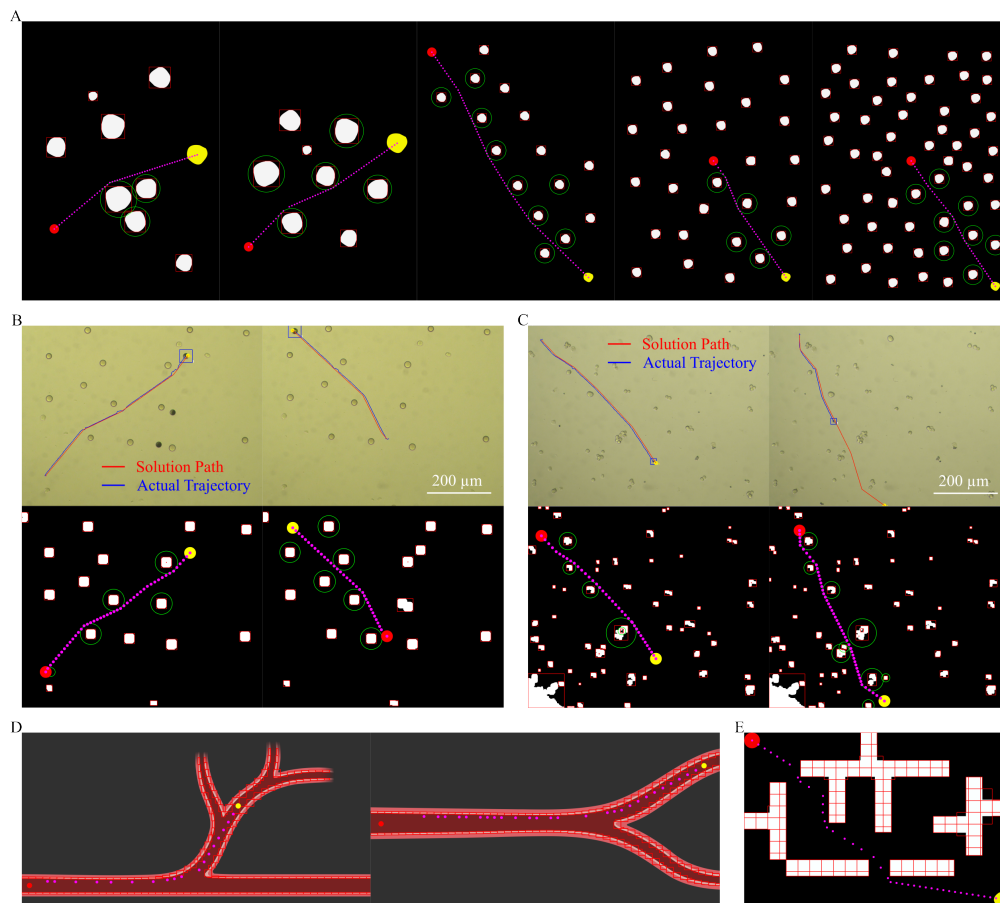


**Figure S5: Additional validation of AGP in static environments.** (A) Simulations with increasing obstacle density. (B) Experiments in a silica particle field: top, bright-field frames overlaid with the AGP solution (red) and measured trajectory (blue); bottom, the corresponding binary masks used for planning. (C) Experiments in a CHO cell field with the same overlays and masks. (D) Simulated vascular phantom with wall boundaries. AGP plans a feasible path while respecting boundary safety zones. (E) Maze-like environment. AGP returns a valid route from start to target.

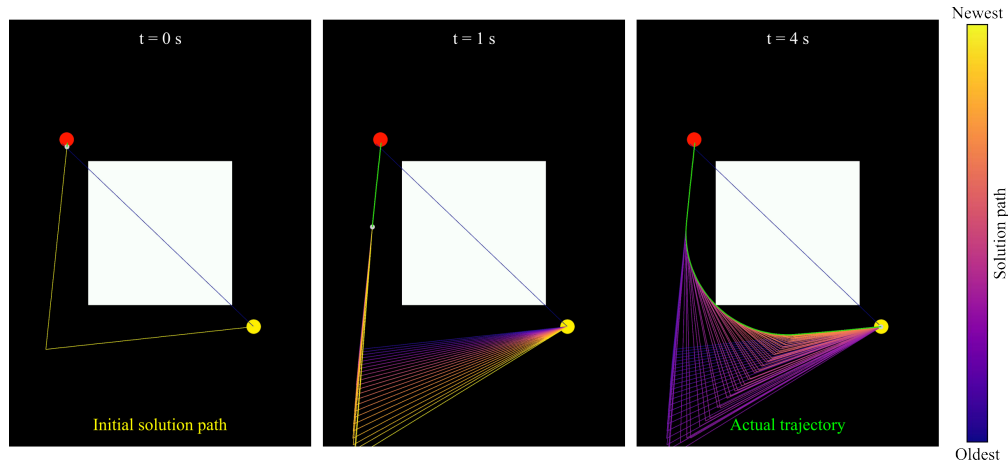


**Figure S6: Real-time AGP shortens the route via online replanning in a static scene.** The plan from the first frame ( $t = 0$  s) is iteratively updated ( $t = 1$  s;  $t = 4$  s), yielding an executed trajectory (green) shorter than the initial solution path. Successive plans are colored from oldest (purple) to newest (yellow).

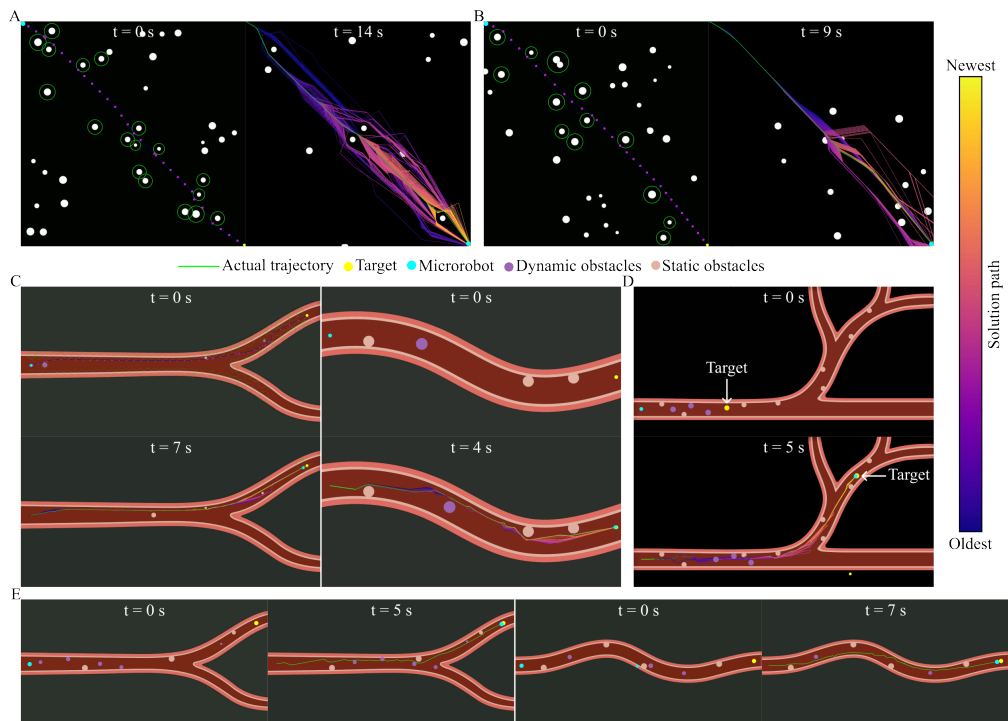


**Figure S7: Simulation results of AGP only (planner without a local controller) for dynamic obstacle avoidance.** (A) Randomly moving obstacles. (B) Obstacles translating with a common direction. (C) Two vascular phantoms with dynamic obstacles. (D) Vascular phantom with a moving target. (E) Two additional, more challenging vascular phantoms with dynamic obstacles.

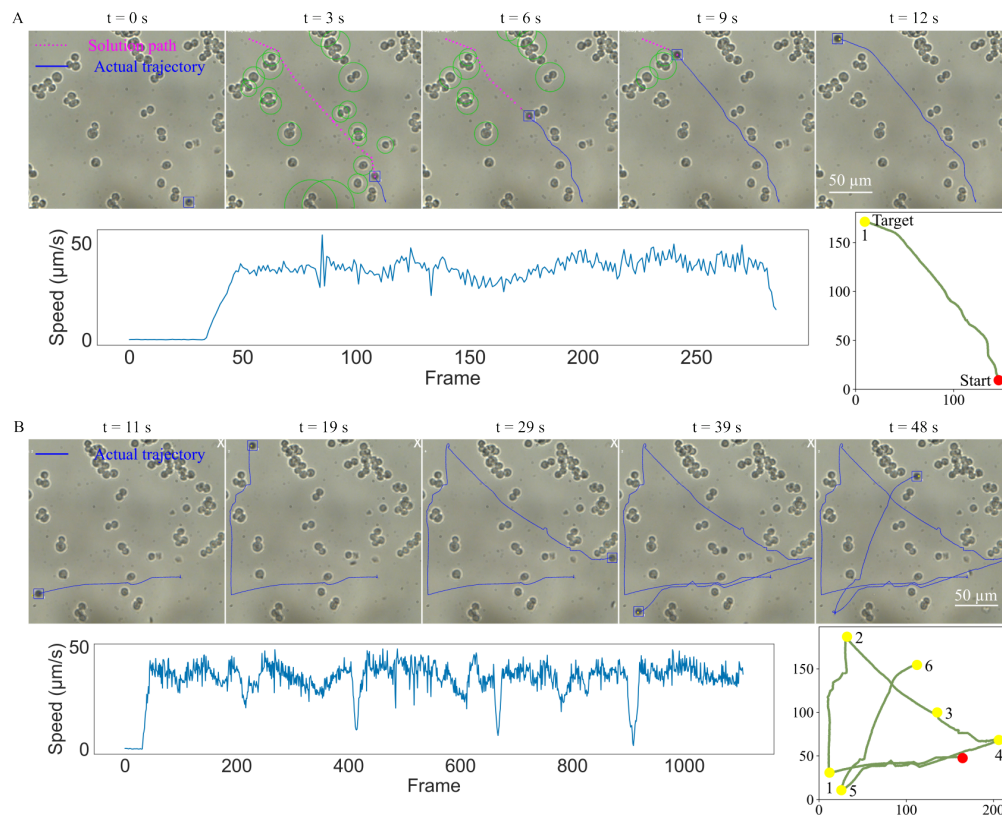


**Figure S8: Additional validation of real-time AGP navigation in a static CHO cell environment.**

Two representative trials are shown: time-lapse brightfield frames with the planned path (pink dots) and actual trajectory (blue), accompanied by speed versus frame plots and the corresponding XY path (right). (A) Single target. (B) Multiple targets.

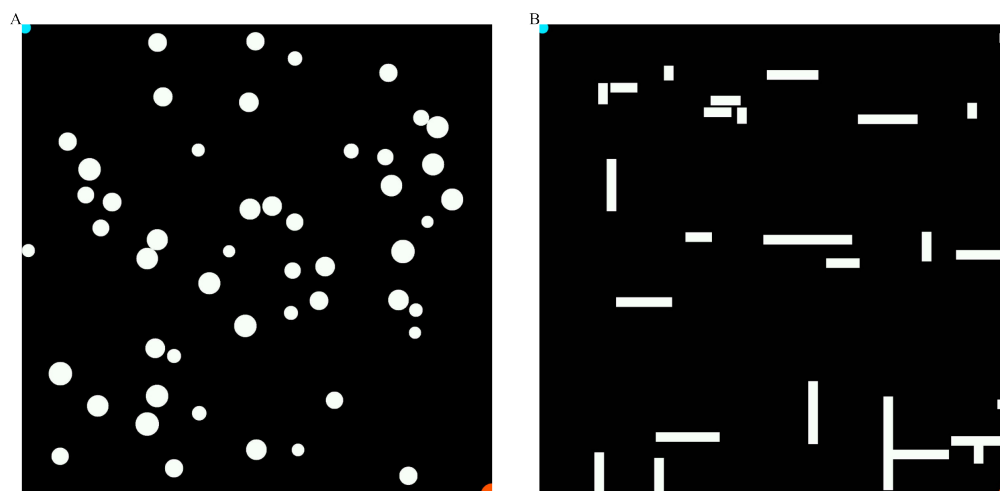


**Figure S9: Additional simulations of AGP with local escape controllers for dynamic obstacle avoidance. (A) Circular obstacles. (B) Rectangular obstacles.**

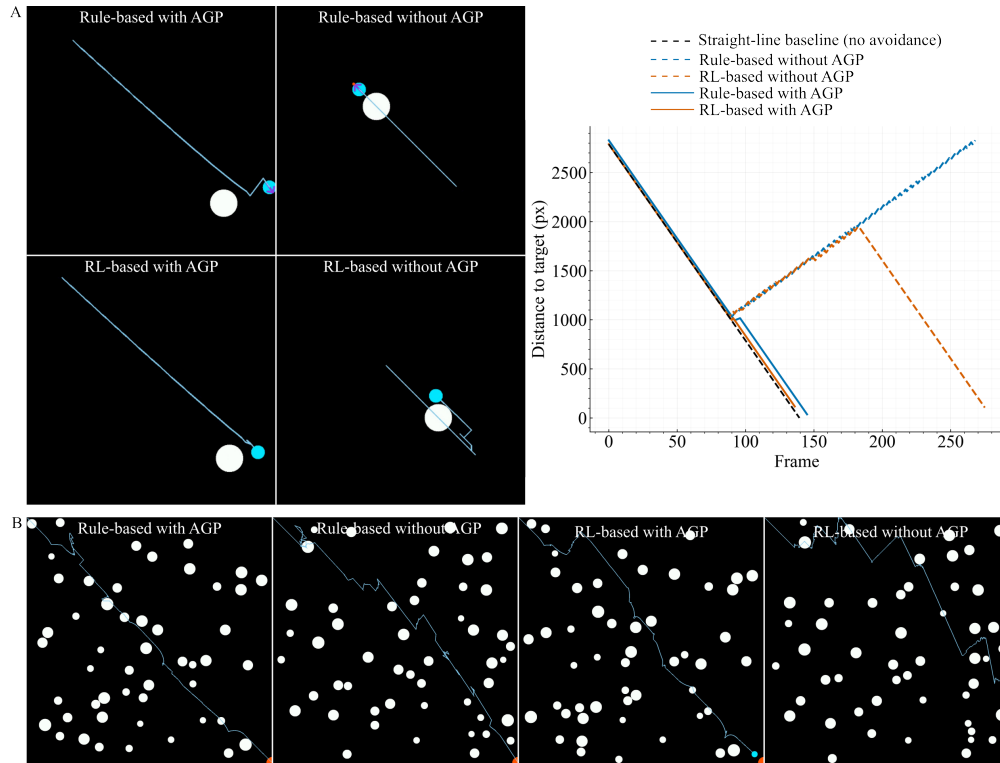


**Figure S10: Dynamic obstacle avoidance using local escape controllers alone versus combined with the global planner (AGP). (A) Single moving circular obstacle (Traces show distance to target with and without AGP). (B) Randomly moving obstacles.**

**Table S3: Helmholtz coil geometry and operating parameters.**

Parameter (Symbol)	Value
Wire gauge	24 AWG copper
Turns per coil ( $N_s, N_m, N_l$ )	$\approx (368, 368, 260)$
Small-pair separation $H_s$ / radius $R_s$	26 mm / 26 mm
Medium-pair separation $H_m$ / radius $R_m$	66 mm / 35 mm
Large-pair separation $H_l$ / radius $R_l$	84 mm / 54 mm
Mounting orientation	small: horizontal; medium/large: vertical

Notes: Radii and separations are measured center to center.

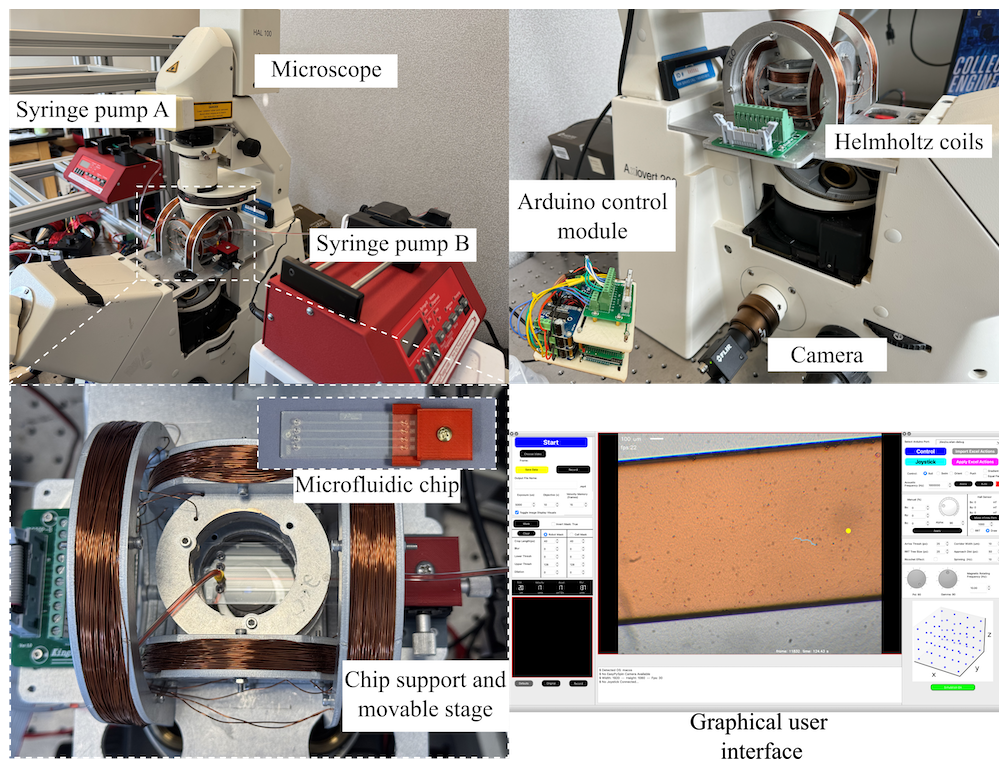


**Figure S11: Experimental setup.** The setup comprises syringe pumps (A, B), an inverted microscope, Helmholtz coils, an Arduino control module, and an imaging camera. The microfluidic chip is mounted on a movable stage within the coil assembly. System operation is monitored and controlled through a custom graphical user interface.

---

### Algorithm 3 2D Analytic Geometry Planner

---

**Require:**  $\mathcal{S}, \mathcal{E} \in \mathbb{R}^2$ ,  $Obstacles = \{(\mathbf{c}_i, r_i)\}_{i=1}^N$ , strip  $\alpha > 0$ , microrobot radius  $R$ , waypoint spacing  $h$

**Ensure:**  $V = [v_1, \dots, v_K]$ ,  $W = [w_1, \dots, w_J]$

```

1:  $\mathbf{s} \leftarrow \mathcal{S}$ ,  $\mathbf{e} \leftarrow \mathcal{E}$ ,  $\mathbf{d} \leftarrow \mathbf{e} - \mathbf{s}$ ;  $r_i \leftarrow r_i + R$ ,  $\forall i$ 
2:  $\mathcal{I}' \leftarrow \emptyset$ ,  $G \leftarrow []$  ▷ Prune by projection and strip
3: for  $i = 1$  to  $N$  do
4:    $t_i \leftarrow \frac{(\mathbf{c}_i - \mathbf{s}) \cdot \mathbf{d}}{\|\mathbf{d}\|^2}$ ,  $\mathbf{g}_i \leftarrow \mathbf{s} + t_i \mathbf{d}$ 
5:   if  $0 \leq t_i \leq 1$  and  $\|\mathbf{c}_i - \mathbf{g}_i\| \leq \alpha r_i$  then
6:     add  $i$  to  $\mathcal{I}'$ ; append  $\mathbf{g}_i$  to  $G$ 
7:   end if
8: end for
9: if  $|\mathcal{I}'| = 0$  then
10:  return  $V = [\mathcal{S}, \mathcal{E}]$ ,  $W = \text{INSERTWAYPOINTS}(V, h)$ 
11: end if
12: sort  $\{(\mathbf{c}_i, r_i, \mathbf{g}_i)\}_{i \in \mathcal{I}'}$  by  $x$  of  $\mathbf{g}_i$ 
13: if  $x_e \neq x_s$  then ▷ Perpendicular family
14:    $k_p \leftarrow -\frac{1}{(y_e - y_s)/(x_e - x_s)}$ 
15: else
16:    $k_p \leftarrow \perp$  to vertical
17: end if
18:  $V \leftarrow [\mathcal{S}]$ ;  $\mathcal{A} \leftarrow \mathcal{I}'$ 
19: while true do
20:   if  $\text{COUNTINTERSECTIONS}(V_{\text{end}}, \mathcal{E}, \mathcal{A}) \leq 1$  then
21:     append  $\mathcal{E}$  to  $V$ ; break
22:   end if
23:    $(p, q) \leftarrow \text{TWO NEAREST}(V_{\text{end}}, \mathcal{A})$ 
24:    $j \leftarrow \text{NEXTFOOTINDEX}(V_{\text{end}}, G, \mathcal{A})$ ;  $L_j \leftarrow$  line through  $\mathbf{g}_j$  parallel to the perpendicular family
25:    $\hat{v} \leftarrow \text{PERPFOOTONLINE}(V_{\text{end}}, L_j)$ 
26:   if  $\text{OUTSIDEALL}(\hat{v}, \mathcal{A})$  then
27:      $v_{\text{new}} \leftarrow \hat{v}$ 
28:   else
29:      $\mathcal{T} \leftarrow \text{TANGENTINTERSECTIONS}(V_{\text{end}}, \{p, q\}, L_j)$ 
30:     if  $|\mathcal{T}| > 0$  then
31:        $v_{\text{new}} \leftarrow \arg \min_{x \in \mathcal{T}} \|x - V_{\text{end}}\|$ 
32:     else if  $q = \emptyset$  then
33:        $v_{\text{new}} \leftarrow \text{SHORTERTANGENTTOLINE}(V_{\text{end}}, p, L_j)$ 
34:     else
35:       break
36:     end if
37:   end if
38:   append  $v_{\text{new}}$  to  $V$ ; remove  $\text{CLOSESTOBSTACLE}(V_{\text{end}}, \mathcal{A})$  from  $\mathcal{A}$ 
39: end while
40:  $W \leftarrow \text{INSERTWAYPOINTS}(V, h)$  ▷ linearly interpolate each segment with spacing  $\approx h$ ; include endpoints
41: return  $V, W$ 

```

---

---

**Algorithm 4** 3D Analytic Geometry Planner

---

**Require:**  $\mathcal{S}, \mathcal{E} \in \mathbb{R}^3$ , obstacles  $\{(\mathbf{C}_m, R_m)\}_{m=1}^M$ , microrobot radius  $R$ , #planes  $n$ , waypoint spacing  $h$

**Ensure:**  $W^{3D} = [w_1^{3D}, \dots, w_J^{3D}] \in \mathbb{R}^{J \times 3}$

```
1:  $\mathbf{d} \leftarrow \mathcal{E} - \mathcal{S}$ ;  $L \leftarrow \|\mathbf{d}\|$ ;  $\hat{\mathbf{d}} \leftarrow \mathbf{d}/L$ 
2:  $\mathbf{q}_0 \leftarrow \text{ORTHONORMALPERP}(\hat{\mathbf{d}})$  ▷ any unit vector orthogonal to  $\hat{\mathbf{d}}$ 
3: for  $i = 1$  to  $n$  do
4:    $\phi_i \leftarrow 2\pi(i - 1)/n$ 
5:    $\mathbf{e}_1 \leftarrow \hat{\mathbf{d}}$ ;  $\mathbf{e}_2 \leftarrow \text{ROTATEAROUND}(\mathbf{q}_0, \hat{\mathbf{d}}, \phi_i)$ ;  $\mathbf{n}_i \leftarrow \mathbf{e}_1 \times \mathbf{e}_2$ 
6:    $\mathcal{O}_i \leftarrow \emptyset$  ▷ 2D circles on plane  $\mathcal{P}_i$ 
7:   for  $m = 1$  to  $M$  do
8:      $r_m^{3D} \leftarrow R_m + R$ ;  $\delta \leftarrow (\mathbf{C}_m - \mathcal{S}) \cdot \mathbf{n}_i$ ;  $d_\perp \leftarrow |\delta|$ 
9:     if  $d_\perp \leq r_m^{3D}$  then ▷ non-empty circle intersection
10:       $\mathbf{P} \leftarrow \mathbf{C}_m - \delta \mathbf{n}_i$ ;  $r_{\text{int}} \leftarrow \sqrt{(r_m^{3D})^2 - d_\perp^2}$ 
11:       $u \leftarrow \mathbf{e}_1^\top (\mathbf{P} - \mathcal{S})$ ;  $v \leftarrow \mathbf{e}_2^\top (\mathbf{P} - \mathcal{S})$ 
12:      if  $0 \leq u \leq L$  then ▷ restrict along the S–E span
13:        add  $((u, v), r_{\text{int}})$  to  $\mathcal{O}_i$ 
14:      end if
15:    end if
16:  end for
17:   $\mathcal{S}^{2D} \leftarrow (0, 0)$ ;  $\mathcal{E}^{2D} \leftarrow (L, 0)$ 
18:   $(W_i^{2D}, L_i) \leftarrow \text{AGP\_2D}(\mathcal{S}^{2D}, \mathcal{E}^{2D}, \mathcal{O}_i, h)$  ▷ returns waypoints and total length
19: end for
20:  $i^* \leftarrow \arg \min_{1 \leq i \leq n} L_i$ 
21: Retrieve  $\mathbf{e}_1, \mathbf{e}_2$  of slice  $i^*$ ;  $W^{3D} \leftarrow []$ 
22: for each  $w = (u, v) \in W_{i^*}^{2D}$  do
23:   append  $w^{3D} \leftarrow \mathcal{S} + u \mathbf{e}_1 + v \mathbf{e}_2$  to  $W^{3D}$ 
24: end for
25: return  $W^{3D}$ 
```

---

---

**Algorithm 5** DQN Training with Global–Local Switch for Dynamic Obstacle Avoidance

---

**Require:** Env:  $(W, H), R, (N_d, N_s), v_m, r_i^{\text{sim}} = r_i + R + \delta; o \in \mathbb{R}^{16}$ ; rewards in Eq. (15)

**Require: Train (Table S2):**  $n_{\text{env}}, N, B, \gamma, S, S_{\text{ini}}, f, K, (\varepsilon_0, \varepsilon_1, \alpha_\varepsilon), \lambda_0, F, M, \mathcal{A}$

- 1: Initialize  $Q_\theta$  with  $\mathcal{A}$  (input 16, output 9); set target  $Q_{\bar{\theta}} \leftarrow Q_\theta$ ; start  $n_{\text{env}}$  parallel envs and logger
  - 2: At episode start, place agent at center and sample a compass direction (*global phase*); while outside all safety zones the env moves autonomously and issues `ignore_transition`
  - 3: **for**  $t = 1, \dots, S$  **do**
  - 4:     **for** each parallel environment  $e = 1, \dots, n_{\text{env}}$  **do**
  - 5:         Observe  $o_t$ ; with prob.  $\varepsilon$  pick random  $a_t$ , else  $a_t = \arg \max_a Q_\theta(o_t, a)$
  - 6:          $(o_{t+1}, r_t, \text{done}, \text{info}) \leftarrow \text{STEP}(a_t)$
  - 7:         **if** `info.ignore_transition` **then**
  - 8:             **continue**
  - 9:         **end if**
  - 10:         Store  $(o_t, a_t, r_t, o_{t+1}, d_{t+1})$  in  $\mathcal{D}$ , where  $d_{t+1} = \#[\text{done}]$
  - 11:         **if** `done` **then**
  - 12:             Reset env (new global direction)
  - 13:         **end if**
  - 14:     **end for**
  - 15:     **if**  $t > S_{\text{ini}}$  **and**  $t \bmod f = 0$  **then**
  - 16:         Sample  $\{(o_j, a_j, r_j, o'_j, d'_j)\}_{j=1}^B \sim \mathcal{D}$
  - 17:          $y_j = r_j + \gamma(1 - d'_j) \max_{a'} Q_{\bar{\theta}}(o'_j, a')$
  - 18:          $\theta \leftarrow \theta - \lambda(t) \nabla_\theta \frac{1}{B} \sum_j \rho_\kappa(y_j - Q_\theta(o_j, a_j))$  ▷ Huber,  $\kappa=1$
  - 19:     **end if**
  - 20:     **if**  $t \bmod K = 0$  **then**
  - 21:          $\bar{\theta} \leftarrow \theta$  ▷ periodic target sync
  - 22:     **end if**
  - 23:     **if**  $t \bmod F = 0$  **then**
  - 24:         Run  $M$  eval episodes; log mean return/length/success
  - 25:         If success  $>$  best so far (or equal with higher return): save snapshot
  - 26:     **end if**
  - 27:     Anneal  $\varepsilon$  and  $\lambda(t)$  per schedules
  - 28: **end for**
  - 29: Save final  $Q_\theta$  and logs
-

**Caption for Movie S1. Experimental validation of AGP in static environments: silica particles and CHO cells.** The video shows two experiments: (i) a  $20\ \mu\text{m}$  magnetic microrobot traveling through a field of  $20\ \mu\text{m}$  silica particles and (ii) a  $4.3\ \mu\text{m}$  microrobot navigating among CHO cells. In each sequence, the AGP planned path (red) is overlaid on the microscope view, and the microrobot's measured trajectory (blue) is drawn as it moves from the start to the yellow target without collision. Animated version of Figure 7(A) and Figure 7(B).

**Caption for Movie S2. Simulation: real-time AGP only (no local escape controller).** The movie compiles six sequences in which only the global planner replans. Static scene: Real-time AGP continuously shortens the route through online replanning (animated version of Figure S6); randomly moving obstacles (animated version of Figure S7(A)); obstacles translating in a common direction (animated version of Figure S7(B)); two vascular phantoms with dynamic obstacles (animated version of Figure S7(C)); a vascular phantom with a moving target (animated version of Figure S7(D)); and more challenging vascular phantoms with dynamic obstacles (animated version of Figure S7(E)).

**Caption for Movie S3. Real-time AGP in biological samples: CHO cell field and microfluidic channel (no flow).** Two experimental sequences are shown. (i) A  $10\ \mu\text{m}$  magnetic microrobot navigates through a CHO cell field using real-time AGP and reaches the target without collision (animated version of Figure 7(C)). (ii) A  $20\ \mu\text{m}$  microrobot moves inside a  $200\ \mu\text{m}$  wide microfluidic channel (no flow) under the same controller (animated version of Figure 7(D)). In both clips, the measured trajectory is traced (blue) and safety zones for detected obstacles are shown (green). The path is replanned every frame.

**Caption for Movie S4. Simulation: local escape controller for fast dynamic obstacles.** Three clips are shown. (i) Rule-based controller: detailed avoidance using symmetric intermediate targets (animated version of Figure 4(B)). (ii) Training environment for RL-based controller (animated version of Figure 5(A)). (iii) RL-based controller: learned policy executing short-range avoidance in a dynamic arena; detours are typically smoother and shorter (animated version of Figure 5(C)).

**Caption for Movie S5. Simulation: comparative performance of local escape controllers.**

The movie compiles several sequences. (i) Fixed and moving targets: side-by-side comparison of three methods: AGP only, AGP with the rule-based controller, and AGP with the RL-based controller (animated versions of Figure 6(A) and (E)). (ii) Additional cluttered scenes with circular and rectangular obstacles using AGP with local controllers (animated versions of Figure S9(A) and (B)). (iii) Vascular phantom with boundary obstacles and static/dynamic circular obstacles (animated version of Figure S9(F)).

**Caption for Movie S6. Dynamic obstacle avoidance: local escape controllers alone vs. with AGP.**

Two sequences compare each local controller run alone (no global planner) against the same controller coupled with the AGP global planner: (i) a single moving circular obstacle (animated version of Figure S10(A)); (ii) multiple randomly moving obstacles (animated version of Figure S10(B)). With AGP, paths are shorter and collisions are avoided.

**Caption for Movie S7. Experimental validation of local escape controllers.**

A  $10\ \mu\text{m}$  magnetic microrobot navigates among black circular dynamic obstacles. In both clips, the AGP global planner replans every frame while (i) the rule-based controller and (ii) the RL-based controller execute short-range avoidance and return the microrobot to the global path. In each experiment the microrobot reaches the target without collision. Animated versions of Figure 7(E) and Figure 7(F).

**Caption for Movie S8. Upstream–steady–downstream transitions of a rolling microrobot in microfluidic channel flow.**

A microrobot rolls in a  $1000\ \mu\text{m}$  wide microfluidic channel under a 20 Hz rotating magnetic field while the flow rate is increased, showing transitions from upstream to steady to downstream.

**Caption for Movie S9. Obstacle avoidance in flow using the RL-based controller (upstream and downstream).**

A  $10\ \mu\text{m}$  microrobot navigates in a  $1000\ \mu\text{m}$  wide microfluidic channel while avoiding flowing human red blood cells and  $10\ \mu\text{m}$  silica particles. The AGP global planner replans every frame and the RL-based local controller performs short-range avoidance, enabling collision-free arrival at the target in both upstream and downstream conditions. Animated version of Figure 7(H).

**Caption for Movie S10. Long-duration autonomous microrobot navigation in microfluidic flow.** A 10  $\mu\text{m}$  microrobot repeatedly traverses a 1000  $\mu\text{m}$  wide channel filled with flowing human red blood cells. Multiple sequential targets are reached in both upstream and downstream segments, demonstrating reliable, stable operation over extended durations with collision-free arrivals.